

# The Statistics of Density Peaks and the Column Density Distribution of the Lyman-Alpha Forest

Lam Hui<sup>1,2</sup>, Nickolay Y. Gnedin<sup>1,3</sup> and Yu Zhang<sup>4</sup>

## ABSTRACT

We develop a method to calculate the column density distribution of the Ly $\alpha$  forest for column densities in the range  $10^{12.5} - 10^{14.5} \text{ cm}^{-2}$ . The Zel'dovich approximation, with appropriate smoothing, is used to compute the density and peculiar velocity fields. The effect of the later on absorption profiles is discussed and it is shown to have little effect on the column density distribution. We introduce an approximation in which the column density distribution is related to a statistic of density peaks (involving its height and first and second derivatives along the line of sight) in real space. We show that the slope of the column density distribution is determined by the temperature-density relation as well as the amount of power on scales  $2 \text{ hMpc}^{-1} \lesssim k \lesssim 20 \text{ hMpc}^{-1}$ . An expression relating the three is given. We find very good agreement between the column density distribution obtained by applying the Voigt-profile-fitting technique to the output of a full hydrodynamic simulation and that obtained using our approximate method for a test model. It is also found that an alternative approximate method which is based on the lognormal approximation tends to underestimate the number of absorption lines at low column densities. The formalism is applied to study a group of CDM as well as CHDM models. Comparison with high resolution Keck data is made.

*Subject headings:* cosmology: theory — intergalactic medium — quasars: absorption lines

---

<sup>1</sup>Department of Physics, Massachusetts Institute of Technology, Cambridge, MA 02139

<sup>2</sup>Center for Theoretical Physics, Laboratory for Nuclear Science, MIT; e-mail: *lhui@space.mit.edu*

<sup>3</sup>Princeton University Observatory, Peyton Hall, Princeton, NJ 08544; e-mail: *gnedin@astro.princeton.edu*

<sup>4</sup>Laboratory for Computational Astrophysics, National Center for Supercomputing Applications, University of Illinois at Urbana-Champaign, Urbana, IL 61801

## 1. Introduction

There is a long history of theoretical efforts to place the study of the Ly $\alpha$  forest within the framework of cosmological structure formation theories (Rees 1986; Bond, Szalay & Silk 1988; McGill 1990; Bi, Börner & Chu 1992). Recent work making use of numerical simulations has greatly advanced our understanding in this direction (Cen et al. 1994; Zhang, Anninos & Norman 1995; Hernquist et al. 1995; Petitjean, Mücket & Kates 1995; Miralda-Escudé et al. 1995). (See also Bi, Ge & Fang 1995, for a linear theory calculation). The emerging picture is that it is possible to account for all the observed properties of the Ly $\alpha$  forest (with column densities less than about  $10^{17} \text{ cm}^{-2}$ ) by assuming it originates from the small scale structure, including the network of filaments, pancakes and mild density fluctuations, which arises naturally in hierarchical clustering cosmological models (Weinberg et al. 1996).

A commonly used statistic to characterize the forest is its column density distribution, the number of absorption lines per unit neutral hydrogen column density per unit redshift as a function of column density. Other useful statistics include line-line correlations and the distributions of  $b$ -values and equivalent widths (Murdoch et al. 1986; Carswell et al. 1991; Press, Rybicki & Schneider 1993; Crisitani et al. 1995). There have also been proposals of new statistical tools (Meiksin and Bouchet 1995; Miralda-Escudé et al. 1995; Pando and Fang 1996). (See Tytler 1992 for a general overview of the statistical issues concerning quasar absorption systems.) We focus our attention on the column density distribution in the present work.

One of the most striking features of the observed column density distribution of quasar absorption systems is that it can be approximated by a single power law that extends over many orders of magnitude. This was emphasized by Tytler (1987), among others, who found that in the range  $10^{13} < N_{\text{HI}} < 10^{22} \text{ cm}^{-2}$ , the distribution was reasonably well represented by a power law,  $\propto N_{\text{HI}}^{-\beta}$  with  $\beta = 1.51 \pm 0.02$ . However, there exists evidence of at least one break. It has been demonstrated that there is a deficit of absorption systems somewhere in the column density range  $10^{14}$  to  $10^{17} \text{ cm}^{-2}$  compared to a power-law extrapolation of the distribution from lower column densities (Carswell et al. 1987; Petitjean et al. 1993; Hu et al. 1995; Giallongo et al. 1996). For reasons that have to do with the nature of the approximations that we make (Sec. 5.1), we focus our attention on absorption systems with column densities in the range  $10^{12.5} < N_{\text{HI}} < 10^{14.5} \text{ cm}^{-2}$ . Hu et al. (1995) obtained  $\beta = -1.46$  with a 95% confidence range of  $(-1.37, -1.51)$  in the column density range  $10^{12.3} < N_{\text{HI}} < 10^{14.5} \text{ cm}^{-2}$ . Lu et al. (1996) found  $\beta = 1.46 \pm 0.06$  for the same range of column densities.

An obvious ultimate goal of recent theoretical work on the Ly $\alpha$  forest is to constrain

theories of structure formation. The natural question is: what determines the normalization and slope of the column density distribution? What are the major determining factors, in addition to the usual parameters specified by a given cosmological model? To answer these questions, another question has to be addressed: what are the analytical and/or computational tools necessary to make accurate predictions for the column density distribution, given all the required parameters?

Accordingly, the present work can be divided into three parts, where the tools are developed, the factors that influence the column density distribution are analyzed and one application to a class of cosmological models is discussed.

Numerical hydrodynamic simulations (Cen et al. 1994; Zhang et al. 1995; Hernquist et al. 1995; Miralda-Escudé et al. 1995) provide the most obvious tools to study the Ly $\alpha$  forest. Computational costs, however, prevent one from testing extensively several cosmological models. We show in this paper that the Zel'dovich approximation (Zel'dovich 1970), with appropriate smoothing, is an efficient and accurate alternative. Our basic assumption is that the part of the Ly $\alpha$  forest with column densities less than about  $10^{14.5} \text{ cm}^{-2}$  arises mostly from regions which are slightly overdense (overdensity  $\lesssim 5$ ) or even underdense and which have not undergone orbit-crossing. The Zel'dovich approximation can be coupled with the equations governing the thermal and ionization states of the gas to yield predictions for the density of neutral hydrogen and the peculiar velocity as a function of position. Absorption spectra are then generated and analyzed. Basic expressions for the absorption optical depth are presented in Sec. 2 and the approximations that go into its computation are discussed in Sec. 3.

Given an absorption spectrum, the column density distribution depends on the methods of identifying lines and assigning column densities. This is discussed in Sec. 4.1. We investigate the effects of peculiar velocities on the column density distribution, using a method described by Miralda-Escudé (1995). We find that although peculiar velocities can strongly influence the shapes of absorption profiles, they play a relatively minor role in determining the column density distribution. The various interesting effects of peculiar velocities are discussed in Sec. 4.2. Motivated by this finding, a very different way of assigning column densities is introduced in Sec. 5, in which no absorption spectrum needs to be generated. In the absence of peculiar velocities, there is a one-to-one correspondence between density peaks in real space (if they are separated by a distance larger than a minimum corresponding to the thermal broadening width) and minima of transmission (maxima in absorption) in the observed spectrum. Under such conditions, we can simply associate each density peak in real space with an absorption line and assign a column density to each based on the height and curvature of the peak. The column density

distribution is then a statistic of density peaks in real space. We apply this procedure (we call it the Density-Peak-Ansatz) to the density field predicted by the truncated Zel'dovich approximation and test the result against that of a full hydrodynamic simulation. The column density distribution obtained in this way is compared to that obtained from the hydrodynamic simulation using the Voigt-profile-fitting-technique, which is the line-identification method most widely used. The level of agreement is found to be excellent. In Sec. 5.1, we discuss the range of parameters in which our computed column density distribution is expected to be reliable.

Armed with the right tools, we turn our attention to the second question: what factors determine the column density distribution? They can be divided into two categories. One has to do with properties of the intergalactic medium, including its temperature, the equation of state or temperature-density relation, the ionizing radiation intensity and the baryon density. Uncertainties in all of them have to be taken into account before one can meaningfully confront theories with observations. We distinguish between the factors that mostly affect the normalization of the column density distribution and those that mostly affect its slope. It is also emphasized that the temperature and the equation of state depend on the reionization history of the universe (a fuller discussion of this point and related topics will be given in a separate paper). The second set of factors affecting the column density distribution has to do with the specific cosmological model, namely the normalization and shape of the corresponding power spectrum. We study a few variants of the Cold Dark Matter (CDM) model in Sec. 6 for this purpose. It is found that the amount of linear power on comoving scales of around  $2 h \text{ Mpc}^{-1}$  to  $20 h \text{ Mpc}^{-1}$  is the single most important factor in determining the slope of the column density distribution (the equation of state also has a weak effect on it). Increasing the power tends to flatten the distribution in the column density range about  $10^{12.5}$  to  $10^{14.5} \text{ cm}^{-2}$ . In Sec. 7, we introduce an expression relating the slope of the column density distribution to the equation of state and the amount of power on small scales.

We then study a class of Cold plus Hot Dark Matter (CHDM) models in Sec. 8, making use of the insights gained in Sec. 6. The  $\Omega_\nu = 0.2$  (density parameter in neutrino) models have steeper column density distributions compared to those with  $\Omega_\nu = 0.1$  because they have less power on the relevant scales. In particular, the low Hubble constant ( $H_0 = 50 \text{ km s}^{-1} \text{ Mpc}^{-1}$ )  $\Omega_\nu = 0.2$  models predict slopes that are steeper than the observed one for most of the parameter-space specifying the properties of the intergalactic medium. Only for equations of state that are close to isothermal can the two be made consistent with each other. We emphasize however that a more detailed comparison between the models and observations, taking fully into account instrumental noise and biases of the line-identification method(s), is necessary before one can firmly reject any model. We

conclude in Sec. 9 .

On our notations, bold faced letters are reserved for three-dimensional vectors. The symbols  $\mathbf{v}_{\text{pec}}$  and  $\mathbf{x}$  denote the three-dimensional peculiar velocity and comoving position while  $v_{\text{pec}}$  and  $x$  are their counterparts along the line of sight of interest. Standard symbols are used for cosmological parameters:  $H$  for the Hubble constant as a function of  $z$ ,  $H_0$  for the Hubble constant today,  $h$  for  $H_0/100 \text{ kms}^{-1}\text{Mpc}^{-1}$ ,  $\Omega_0$  for the density parameter today, with the subscript  $b$  to denote its baryon portion and  $\nu$  its neutrino content. We use the symbol  $h$  (in distinct from  $h$ ) to denote the Planck constant in a few places where it arises. The term multiple-streaming is reserved for the situation where a single observed redshift corresponds to more than one position in real space. We distinguish it from the term orbit-crossing, which is commonly used interchangeably with multiple-streaming in other contexts. Orbit-crossing refers to the case where a single position has more than one velocity.

## 2. Cosmological Lyman-Alpha Absorption in a Fluctuating Medium: Basic Results

A photon emitted with energy higher than 10.196 eV (wavelength of  $1216 \text{ \AA}$ ) by a distant quasar is continuously redshifted as it travels through the intergalactic medium until it reaches the observer. At some intermediate point, the photon is redshifted to around  $1216 \text{ \AA}$  in the rest frame of the intervening medium, which may contain neutral hydrogen. It can then excite the  $\text{Ly}\alpha$  transition and be absorbed. Let us consider a particular line of sight from the observer to the quasar. The optical depth  $\tau$  (the probability of transmission is given by  $e^{-\tau}$ ) of a photon at a given observed frequency  $\nu_O$  is given by:

$$\tau(\nu_O) = \int_{x_A}^{x_B} n_{\text{HI}} \sigma_\alpha \frac{dx}{1+z}, \quad (1)$$

where  $x$  is the comoving radial coordinate of some intermediate point along the line of sight,  $z$  is the redshift and  $n_{\text{HI}}$  is the proper number density of neutral hydrogen at that point. The limits of integration,  $x_A$  and  $x_B$ , are the comoving positions of the observer and the quasar. The  $\text{Ly}\alpha$  absorption cross-section is denoted by  $\sigma_\alpha$ . It is a function of the frequency of the photon with respect to the rest frame of the intervening hydrogen at position  $x$ . Let us call this frequency  $\nu$ . The cross-section is peaked when  $\nu$  is equal to the  $\text{Ly}\alpha$  frequency,  $\nu_\alpha$ .

The frequency  $\nu$  is related to the observed frequency  $\nu_0$  by:

$$\nu = \nu_0 (1 + \bar{z}) \left( 1 + \frac{v_{\text{pec}}}{c} \right), \quad (2)$$

where  $v_{\text{pec}}$  is the peculiar velocity along the line of sight at position  $x$  and  $1+z$  is the redshift factor *due to the uniform Hubble expansion alone* at the same position. The peculiar velocity of the observer, which merely displaces the whole spectrum by a constant amount (independent of  $x$ ), is ignored. The quantity  $v_{\text{pec}}/c$ , where  $c$  is the speed of light, is much smaller than 1.

It proves convenient for later discussion to expand  $z$  around some mean redshift of interest  $\bar{z}$ , which could be the redshift of a simulation output or the average redshift of an observed spectrum with limited redshift range. Using  $dx = cdt/a$ , where  $a$  is the Hubble scale factor and  $t$  is the proper time, it can be shown that

$$\nu = \nu_0(1+z) \left(1 + \frac{u}{c}\right), \quad u \equiv \frac{\bar{H}}{1+\bar{z}}(x-\bar{x}) + v_{\text{pec}}(x), \quad (3)$$

where  $\bar{x}$  is the position at which the redshift due to Hubble expansion coincides exactly with  $\bar{z}$ . The Hubble constant at the same redshift is denoted by  $\bar{H}$ . We assume the range of  $x$  is small enough so that  $u/c \ll 1$ . The convention  $a = 1$  today is adopted.

The velocity coordinate  $u$  defined above contains contributions from both the Hubble expansion and the peculiar motion. Without peculiar motion,  $u$  increases monotonically with  $x$  and is in fact linear in  $x$ . Peculiar velocities destroy the linear relation and could give rise to situations where a given  $u$  corresponds to more than one position  $x$ . It implies that a photon of a given observed frequency  $\nu_0$  can have the same rest-frame frequency  $\nu$  at more than one place in its trajectory from the quasar to the observer. We reserve the term multiple-streaming to this situation and distinguish it from orbit-crossing where a given  $x$  carries more than one  $v_{\text{pec}}$  or  $u$ . We will return to the subject of multiple-streaming in Sec. 4.2 and that of orbit-crossing in Sec. 3.1.

We define one more velocity coordinate  $u_O$ , which is related to the observed frequency  $\nu_O$  by:

$$\nu_O = \frac{\nu_\alpha}{1+\bar{z}} \left(1 - \frac{u_O}{c}\right) \quad (4)$$

where  $\nu_\alpha$  is the Ly $\alpha$  frequency. The velocity coordinate  $u_0$  is simply equal to  $u$  when  $\nu$  coincides exactly with  $\nu_\alpha$  (this can be seen by comparing eq. [3] and [4], bearing in mind that  $u/c$  and  $u_0/c$  are both assumed to be much less than 1).

With the definitions in place, we change the variable from  $x$  to  $u$  in equation (1), which results in the following expression for  $\tau$ , now a function of  $u_O$ :

$$\tau(u_O) = \sum \int_{u_A}^{u_B} \frac{n_{\text{HI}}}{1+z} \left| \frac{du}{dx} \right|^{-1} \sigma_\alpha du, \quad \sigma_\alpha = \sigma_{\alpha 0} \frac{c}{b\sqrt{\pi}} e^{-(u-u_O)^2/b^2}. \quad (5)$$

The summation refers to a sum over multiple-streams (all the  $x$ 's within the range  $x_A - x_B$  that corresponds to a given  $u$ ), and  $n_{\text{HI}}$ ,  $z$  and  $|du/dx|^{-1}$  are now functions of  $u$ . The limits

of integration  $u_A$  and  $u_B$  are the velocity coordinates corresponding to the positions  $x_A$  and  $x_B$  (assuming no orbit-crossing so that each  $x$  carries one  $u$ ). Note that in practice, only a limited range of  $u$  contributes to  $\tau$  for a limited range of  $u_O$  so that one can replace the redshift  $z$  with  $\bar{z}$ . The same is also true for equation (1).

The Ly $\alpha$  cross-section is expressed as a function of  $u - u_O$ . The constant  $\sigma_{\alpha 0}$  is equal to the combination of fundamental physical constants  $0.416\pi q^2/(m_e c v_\alpha)$ , where  $q$  is the charge of an electron and  $m_e$  is its mass. It is about  $4.5 \times 10^{-18} \text{ cm}^2$ . The parameter  $b$  is equal to  $\sqrt{2k_B T/m_p}$  where  $k_B$  is the Boltzmann constant,  $m_p$  is the mass of a proton and  $T$  is the temperature of the gas.

The form of the line profile function above takes into account thermal broadening but ignores the natural line width. A more general profile function involves a convolution of the two, resulting in the Voigt profile (Rybicki & Lightman 1979). However, for column density less than about  $10^{17} \text{ cm}^{-2}$ , the simple thermal profile is adequate. Only for systems where the optical depth greatly exceeds one is it important to use the full Voigt profile. The reader is referred to Spitzer (1978) and Press and Rybicki (1993) for discussions of curve of growth analysis.

Note also that it is sometimes assumed  $b$  contains a component due to turbulent motion. We do not include it explicitly in our formalism. Bulk motion, on the other hand, is accounted for by  $v_{\text{pec}}$  or  $u$ .

Let us consider two different limits of equation (5).

Suppose there is a high local maximum in  $n_{\text{HI}}|du/dx|^{-1}$  at some  $u = u_{\text{max}}$  with width in velocity space much smaller than the thermal width  $b$ . Then one can take the line profile function associated with  $\sigma_\alpha$  out of the integral in equation (5) because  $n_{\text{HI}}|du/dx|^{-1}$  varies much more rapidly than the thermal profile:

$$\tau(u_O) = \left( \int_{\text{max}} n_{\text{HI}}(x) \frac{dx}{1+z} \right) \sigma_{\alpha 0} \frac{c}{b\sqrt{\pi}} e^{-(u_O - u_{\text{max}})^2/b^2}, \quad (6)$$

where the variable of integration has been changed back from  $u$  to  $x$ . The equation holds when  $u_O$  is close enough to  $u_{\text{max}}$ . The integral is over the local maximum, assuming that the amount of neutral hydrogen away from the maximum does not cause significant absorption (until another maximum is encountered). One then sees an absorption line with an exponential profile in optical depth. While the width of the line tells us about  $b$ , which is proportional to the square root of the temperature, the depth of the line provides information about both  $b$  and the column density, which is the integral inside the first pair of brackets on the right hand side. Let us call this the narrow-maximum-limit.

Consider another limit of the integral (eq. [5]) in which  $n_{\text{HI}}|du/dx|^{-1}$  varies slowly with

*u.* Suppose the scale of variation is much larger than the thermal width. In this case, one can leave the line profile function inside the integral but take the rest outside:<sup>5</sup>

$$\tau(u_O) = \sum \frac{n_{\text{HI}}}{1 + \bar{z}} \left| \frac{du}{dx} \right|^{-1} c \sigma_{\alpha 0}. \quad (7)$$

The velocity dependent terms on the right hand side are evaluated at  $u_O$ . The profile function has been integrated out.

In the above limit,  $\tau$  does not necessarily have the thermal profile around its maxima. We will call this the broad-maximum-limit. An extreme example is that of a homogeneous medium, which gives rise to featureless and uniform absorption (Gunn & Peterson 1965).

Conventional analysis of quasar spectra involves identifying those parts of the spectra that are due to the Ly $\alpha$  absorption and fitting them with superpositions of the Voigt profiles (of which the thermal profiles are a subset) until the residual signal is consistent with noise. This technique was motivated by the picture of the intergalactic medium as consisting of a smooth component which causes relatively little absorption and a set of clouds that satisfy the narrow-maximum-limit. For each cloud, the best-fit Voigt profile then yields its temperature and column density according to equation (6).

However, it is clear that for a general fluctuating medium, not all maxima in  $\tau$  necessarily satisfy the conditions leading to equation (6). In fact, according to most structure formation theories, there invariably exists fluctuations in the intergalactic medium on scales larger than the thermal width. In the broad-maximum-limit, the shape of a local maximum in optical depth is determined by the distributions of  $n_{\text{HI}}$  and  $|du/dx|$  around it. Each maximum in  $\tau$  can still be identified as an absorption line and one can even apply standard techniques and try to fit its shape with superposition of the Voigt profiles. Given the best-fit Voigt profiles, one can assign a *b*-value (width of the profile) and a column density to each profile but it is no longer true, for instance, that the *b*-value thus obtained is equal to  $\sqrt{2k_B T/m_p}$  (eq. [5]). A reasonable question to ask is whether there are other practical methods of identifying absorption lines and assigning column densities without assuming every absorption line consists of a superposition of the Voigt profiles. This will be discussed in Sec. 4.1. It should be borne in mind, however, that all existing observational data on the column density distribution are obtained using the Voigt-profile-fitting-technique, so for the purpose of comparing theory with observations, it is important the line-identification algorithm one uses gives results consistent with the profile-fitting-technique.

---

<sup>5</sup>The expression is not valid at velocity caustics, where  $du/dx$  vanishes. Further discussion on velocity caustics can be found in Sec. 4.2.

In general, there are regions of high density and limited extent, galaxies for instance, which give rise to absorption profiles well approximated by the narrow-maximum-limit, but there are also regions in the intergalactic medium with gentle fluctuations where the broad-maximum-limit holds. Then there are those places where neither limit applies, in which cases, a full integration of equation (5) has to be carried out to compute the optical depth. To do so, one needs to know how the neutral hydrogen density, peculiar velocity and temperature vary with space. This is the subject of the next section. In any case, the above discussion should make it clear that the quasar absorption spectrum contains a wealth of information on the intergalactic medium.

### 3. Ingredients for Generating Quasar Absorption Spectra

There are four quantities that go into the computation of the optical depth: temperature, peculiar velocity, overdensity and neutral fraction. That the temperature and peculiar velocity are important should be obvious from the expression for the absorption cross-section in equation (5). The temperature determines the extent of thermal broadening ( $b$ ) and the peculiar velocity changes the frequency of the photon in the fluid rest-frame (eq. [3]). Let us define carefully what we mean by the other two quantities, the overdensity and the neutral fraction.

Suppose  $n_H(\mathbf{x})$  is the total proper number density of all hydrogen species at position  $\mathbf{x}$  and  $\bar{n}_H$  is its spatial average. The overdensity  $\delta_b$ , which describes the variation in space of  $n_H(\mathbf{x})$ , satisfies:

$$n_H(\mathbf{x}) = \bar{n}_H [1 + \delta_b(\mathbf{x})] , \quad \rho_b(\mathbf{x}) = \bar{\rho}_b [1 + \delta_b(\mathbf{x})] . \quad (8)$$

In the first expression,  $\delta_b$  is defined as the number overdensity of hydrogen. In the second expression, we equate  $\delta_b$  with the mass overdensity of baryons ( $\rho_b$  is the proper mass density of baryons and  $\bar{\rho}_b$  is its mean), which is an excellent approximation for our application because there is no significant conversion of hydrogen into other elements, nor is there any interaction that could cause the spatial distribution of hydrogen to deviate significantly from that of other types of baryons.

What the Ly $\alpha$  absorption directly probes is not the total hydrogen density but its neutral component. The neutral fraction  $X_{\text{HI}}$  is defined by the following relation:

$$n_{\text{HI}}(\mathbf{x}) = n_H(\mathbf{x}) X_{\text{HI}}(\mathbf{x}) , \quad (9)$$

where  $n_{\text{HI}}$  is the proper number density of neutral hydrogen as a function of space. The neutral fraction is determined by the balance between recombination and ionization, the rates of which are dictated by the temperature and radiation intensity respectively.

In general, all four quantities, overdensity  $\delta_b$ , peculiar velocity  $v_{\text{pec}}$ , temperature  $T$  and neutral fraction  $X_{\text{HI}}$ , are functions of position. In the next two sub-sections, we discuss first how to determine the spatial distributions of  $\delta_b$  and  $v_{\text{pec}}$ , and second how  $T$  and  $X_{\text{HI}}$  vary with position through their dependence on  $\delta_b$ . All quantities are evaluated at  $\bar{z} = 3$ . Although most of the material in this section is standard textbook fare, it consists of a somewhat unusual combination of methods, so it is worth going through the basic equations and stating our assumptions carefully.

### 3.1. The Zel'dovich Approximation

In cosmological models where dark matter (a term we use interchangeably with non-interacting matter) dominates the mass density of the universe,  $\delta_b$  as defined in equation (8) coincides with the dark matter overdensity  $\delta_{\text{DM}}$  on large scales. We define  $\delta_{\text{DM}}$  in an analogous manner as before (eq. [8]):

$$\rho_{\text{DM}}(\mathbf{x}) = \bar{\rho}_{\text{DM}}[1 + \delta_{\text{DM}}(\mathbf{x})], \quad (10)$$

where  $\rho_{\text{DM}}$  is the mass density of dark matter at position  $\mathbf{x}$  and  $\bar{\rho}_{\text{DM}}$  is its mean. The equality  $\delta_b = \delta_{\text{DM}}$  is equivalent to the statement that the hydrogen density (which we assume is simply proportional to the baryon density) varies with position in the same manner as the dark matter density does. This is true on large scales where gas pressure is insignificant compared to the gravitational attraction of the dark matter, provided the baryons and dark matter start out having the same spatial distribution, which is true for most popular cosmological models. Moreover, with no significant interaction that distinguishes between the two on large scales, the baryons and dark matter share the same peculiar velocity field. On small scales, however, gas pressure can cause the spatial distributions of baryons and dark matter and their velocities to differ. We will return to this point below.

Hence, on sufficiently large scales (how large is large, an obviously important question, will be addressed later), it is adequate to know the overdensity and peculiar velocity of the dark matter. The Zel'dovich approximation (Zel'dovich 1970) is a well-tested approximation to compute the density and velocity distributions of dark matter in the mildly nonlinear regime ( $\delta_{\text{DM}} \lesssim 5$ ) before orbit-crossing. The reader is referred to the article by Shandarin and Zel'dovich (1989) for a comprehensive review (see also Hui and Bertschinger 1996 for an alternative formulation of the approximation).

The starting point of the Zel'dovich approximation is the following equation for the

displacement of a given mass element or particle:

$$\mathbf{x}(\mathbf{q}, t) = \mathbf{q} + D_+(t) \nabla_{\mathbf{q}} \psi(\mathbf{q}), \quad (11)$$

The coordinate  $\mathbf{q}$  is the initial position of the mass element and  $\mathbf{x}$  is its comoving position as a function of time. The displacement is then  $D_+(t) \nabla_{\mathbf{q}} \psi(\mathbf{q})$ . Its time dependent part  $D_+(t)$  is the linear growth factor (Peebles 1980), which, for a universe with critical matter density, can be equated with  $a$ , the Hubble scale factor. The time independent function  $\nabla_{\mathbf{q}} \psi(\mathbf{q})$  is determined by initial conditions. Growing mode initial conditions dictate that it is curl-free, hence its form as the gradient of the potential  $\psi$  ( $\nabla_{\mathbf{q}}$  is the spatial gradient in  $q$  space).

Expressions for the peculiar velocity and overdensity follow immediately from equation (11):

$$\mathbf{v}_{\text{pec}} = a \dot{D}_+ \nabla_{\mathbf{q}} \psi, \quad 1 + \delta_{\text{DM}} = \det^{-1} \left[ \delta_{ij} + D_+(t) \frac{\partial^2 \psi}{\partial q_i \partial q_j} \right]. \quad (12)$$

The dot in the first expression denotes differentiation with respect to proper time  $t$ . The peculiar velocity is defined by  $\mathbf{v}_{\text{pec}} = a d\mathbf{x}/dt$ . The second expression follows from mass conservation i.e.  $(1 + \delta_{\text{DM}}) d^3 x = d^3 q$ . The right hand side of the second expression is simply the Jacobian of the  $q$ - $x$  transformation matrix.

The function  $\psi(\mathbf{q})$  contains all the information on the specific cosmological model one chooses to study. For the cosmological models we study in this paper, it is a Gaussian random field in  $\mathbf{q}$  space. Suppose  $\tilde{\psi}(\mathbf{k})$  is its Fourier counterpart defined by  $\psi = \int d^3 k \tilde{\psi} e^{i\mathbf{k} \cdot \mathbf{q}}$ . The two-point correlation of  $\tilde{\psi}$  is related to the commonly used power spectrum  $P$  by

$$\langle \tilde{\psi}(\mathbf{k}) \tilde{\psi}^*(\mathbf{k}') \rangle = k^{-4} P(k) \delta^3(\mathbf{k} - \mathbf{k}'), \quad (13)$$

where  $P$  is related to the root-mean-squared (rms) linear overdensity fluctuation by

$$\langle \delta^2 \rangle = D_+^2(t) \int_0^\infty 4\pi P(k) k^2 dk. \quad (14)$$

Note that  $D_+^2 = (1 + \bar{z})^{-2}$  for a universe with critical matter density, choosing  $D_+ = 1$  today.

To produce a realization of the density and velocity fields for a given cosmological model, we employ the following procedure: first, we use the corresponding power spectrum to generate the Gaussian random field  $\psi(\mathbf{q})$  on a grid; second, we displace particles from their initial grid positions ( $\mathbf{q}$ ) according to equation (11) for  $D_+(t)$  corresponding to  $\bar{z} = 3$ ; third, a peculiar velocity is assigned to each particle according to the first expression in equation (12); finally, we use the TSC (Triangular-Shaped density Cloud) scheme (Hockney

& Eastwood 1988) to interpolate the particle positions and velocities to become momentum and mass densities on the grid and divide one by the other to obtain the velocity itself. The interpolation to obtain mass density is our way of enforcing mass conservation, as is expressed in the second expression of equation (12). In the last procedure, we smooth the momentum and mass density fields over a small number of grid cells (in fact, we use one and have checked that the precise number is not important as long as it is small) before performing the division to obtain the velocity field so that we have well-defined velocities even in places with zero density after the TSC interpolation (Kofman et al. 1994). Any line of sight can then be chosen through the simulation box and the above set of steps gives the overdensity and peculiar velocity (in fact only the component parallel to the line of sight is needed) at each grid point on it.

The procedure just outlined is very efficient because there is no need to integrate any equation of motion. One simply multiply the displacement of each particle by an appropriate factor of  $D_+(t)$ . However, the first step of the procedure has to be slightly modified to address two problems.

The first one is orbit-crossing. The Zel'dovich approximation is known to predict too rapid growth of the thickness of the post-collapse pancake (Shandarin and Zel'dovich 1989). A number of cures have been proposed (Kofman, Pogosyan, & Shandarin 1990; Matarrese et al. 1992; Brainerd, Scherrer, & Villumsen 1993; Bagla & Padmanabhan 1994) but the one that consistently gives good agreement with N-body simulations is the truncated Zel'dovich approximation (Coles, Melott & Shandarin 1993; Melott, Buchert & Weiß 1995). The basic idea is to smooth the initial power spectrum on small scales so that the amount of orbit-crossing that might have occurred by the time of interest is not significant enough to destroy the accuracy of the Zel'dovich approximation on large scales, where the fluctuations are still mildly nonlinear. The initial power spectrum  $P(k)$  is multiplied by a Gaussian smoothing kernel of the form  $e^{-k^2/k_S^2}$ , before it is used to generate the Zel'dovich displacement field (eq. [13]). The smoothing wavenumber  $k_S$  is chosen according to the following prescription

$$k_S = 1.5 k_{NL}, \quad \text{where } 1 = D_+^2(t) \int_0^{k_{NL}} 4\pi P(k) k^2 dk. \quad (15)$$

Note that  $P(k)$  above is the initial power spectrum before any smoothing. The proportionality constant between  $k_S$  and  $k_{NL}$  actually depends somewhat on the power spectrum, with more smoothing (smaller  $k_S$ ) required for models that have relatively more power on small scales (Melott 1994). The choice above has been shown to give good agreement with N-body simulations for CDM models (Melott et al. 1995). We will see that for those CHDM models with relatively little power on small scales, the precise value

of  $k_S$  is not important. The procedure described above is commonly called the truncated Zel'dovich approximation.

The second problem is one we have pointed out before, namely that  $\delta_{\text{DM}}$  is not necessarily equal to  $\delta_b$  (which is what we are interested in ultimately) on small scales. In linear theory, it is possible to show that for a dark matter dominated universe, the Fourier components of the two quantities obey  $\tilde{\delta}_b(k) = \tilde{\delta}_{\text{DM}}(k)$  when  $k \ll k_J$  and  $\tilde{\delta}_b(k) = k_J^2 \tilde{\delta}_{\text{DM}}(k)/k^2$  when  $k \gg k_J$ . Under some restrictive assumptions (see Appendix A), it can be shown that  $\tilde{\delta}_b(k) = \tilde{\delta}_{\text{DM}}(k)(1 + k^2/k_J^2)^{-1}$ . The quantity  $k_J^{-1}$  is known as the Jeans scale and is defined by:

$$k_J^{-1} = \sqrt{\frac{\gamma k_B \bar{T}}{4\pi a^2 G \mu \bar{\rho}_{\text{DM}}}}, \quad (16)$$

where  $k_B$  is the Boltzmann constant,  $\bar{T}$  is the spatially averaged temperature of the gas,  $\mu$  is the mean mass per particle (for fully ionized gas with primordial abundances, it is about  $0.6m_p$  where  $m_p$  is the mass of the proton) and  $\gamma$  describes the relation between the temperature  $T$  (the actual, not average, value) and  $1 + \delta_b$ :  $T \propto (1 + \delta_b)^{\gamma-1}$ . Note that  $\gamma$  does not necessarily equal  $5/3$  unless the gas behaves adiabatically. The proofs of the above assertions can be found in the Appendix A (see also Bi et al. 1992; Peebles 1993). It is sufficient to note here that in the linear regime, the baryon density field is smoother than that of the dark matter on small scales due to the effect of gas pressure.

Now, the above relations between  $\tilde{\delta}_b$  and  $\tilde{\delta}_{\text{DM}}$  hold only in the linear regime when both quantities are small. To take into account the effect of gas pressure in the mildly nonlinear regime, one possibility is to smooth the initial power spectrum by a factor of  $(1 + k^2/k_J^2)^{-2}$  before generating the displacement field, similar to what is done in the case of the truncated Zel'dovich approximation. This method was used by Reisenegger & Miralda-Escudé (1995) to study the fluctuating Gunn-Peterson effect. In practice, we smooth the initial power spectrum by a Gaussian kernel  $e^{-k^2/k_J^2}$  and find that the two ways of smoothing give very similar column density distributions.

To give an idea of scale, for  $\gamma = 1.5$ ,  $\bar{T} = 10^4$  K and a universe at critical density,  $k_J$  is equal to  $16.8 h \text{ Mpc}^{-1}$ . It turns out that for all models considered in this paper except the  $\Omega_\nu = 0.2$  CHDM models, the truncation scales  $k_S^{-1}$  according to equation (15) are larger than  $k_J^{-1}$  (eq. [16]), for reasonable ranges of temperature and  $\gamma$ . For these models, it is unnecessary to smooth the initial power spectrum over the Jeans scale because the truncated Zel'dovich approximation already prescribes more smoothing. The opposite is true for the  $\Omega_\nu = 0.2$  CHDM models. In fact, the amount of small scale power is so insignificant for these models that the precise scale of smoothing does not affect the column density distribution for column densities of interest (Sec. 8). Orbit-crossing is probably not

very severe for this class of models. Hence, uncertainty in the Jeans smoothing scale due to uncertainties in the temperature and equation of state of the intergalactic medium is not a concern.

To sum up, we smooth the initial power spectrum on the scale of  $k_S^{-1}$  (eq. [15]) or  $k_J^{-1}$  (eq. [16]), depending on which is bigger, before it is used to generate the displacement field (eq. [13]). The rest of the procedure to obtain the overdensity  $\delta_b$  and peculiar velocity  $v_{\text{pec}}$  on a grid follows as before. The implicit assumption underlying the whole procedure is that fluctuations on scales smaller than the smoothing scale do not contribute significantly to the number of absorption lines at our column densities of interest, about  $10^{12.5} - 10^{14.5} \text{ cm}^{-2}$ . The upper limit is related to the maximum overdensity ( $\delta_b$  around 5) beyond which the Zel'dovich approximation is not expected to be reliable and the lower limit is set by our resolution (see Sec. 5 for more details). We show in Sec. 5 a comparison between the column density distribution computed using the approximate method described here and that using a full hydrodynamic simulation. The level of agreement lends support to our assumption. Another consistency check is to see if shock-heating is important for regions with overdensities (or underdensities) associated with the above range of column densities. A plot of density versus temperature like Fig. 2 in Weinberg et al. (1996) shows that shock-heating, and by extension orbit-crossing, is not important for regions of underdensity or low overdensity.

### 3.2. The Thermal and Ionization State

Given the evolution of  $\delta_b$  predicted by the Zel'dovich approximation, it is possible to integrate evolution equations for  $T$  and for  $X_{\text{HI}}$  as well as the abundance of other species to obtain their relations with  $\delta_b$ .<sup>6</sup>

Details of the computation will be given in a separate paper (Hui and Gnedin 1996). A brief discussion can be found in Appendix B of this paper. We summarize the main relevant conclusions here.

First, ionization equilibrium is maintained at high accuracy except during the period of initial reionization. Ionization equilibrium implies that the neutral hydrogen fraction (eq.

---

<sup>6</sup>Since these equations are local, in the sense that each mass element evolves independently of the others, there is actually no need to generate a full three-dimensional realization for the purpose of studying the thermal and ionization evolution. A simpler approach is to generate a set of eigenvalues of the deformation matrix  $\partial^2\psi/\partial q_i\partial q_j$  according to the prescription of Doroshkevich (1970) and determine the density evolution through the second part of equation (12).

[9]) satisfies

$$X_{\text{HI}} \sim 1.6 \times 10^{-6} \left( \frac{T}{10^4 K} \right)^{-0.7} \left( \frac{\Omega_b h^2}{0.0125} \right) \left( \frac{J_{\text{HI}}}{0.5} \right)^{-1} (1 + \delta_b) \left( \frac{1 + \bar{z}}{4} \right)^3. \quad (17)$$

The quantity  $J_{\text{HI}}$  is a measure of the radiation intensity defined as follows (analogous to the definition in Miralda-Escudé et al. 1995 but differs by a factor of  $10^{-21} \text{ ergsHz}^{-1}\text{s}^{-1}\text{cm}^{-2}\text{ster}^{-1}$ ):

$$J_{\text{HI}} = \frac{\int_{\nu_{\text{HI}}}^{\infty} 4\pi J_{\nu} \sigma_{\text{HI}} \frac{d\nu}{h\nu}}{\int_{\nu_{\text{HI}}}^{\infty} 4\pi \sigma_{\text{HI}} \frac{d\nu}{h\nu}} (10^{-21} \text{ ergsHz}^{-1}\text{s}^{-1}\text{cm}^{-2}\text{ster}^{-1})^{-1}, \quad (18)$$

where  $J_{\nu}$  is the specific intensity as a function of frequency  $\nu$  in the units given above,  $h$  is the Planck constant,  $h\nu_{\text{HI}}$  is 13.6 eV and  $\sigma_{\text{HI}}$  is the ionization cross-section. The photo ionization rate is simply equal to  $4 \times 10^{-12} J_{\text{HI}} \text{ s}^{-1}$  which is the number of ionization per unit time.

Observations indicate that  $J_{\text{HI}}$  is between about 0.1 and 2.0 for  $\bar{z} = 2 - 4$  (Bechtold 1994; Batjlik, Duncan & Ostriker 1988; Lu et al. 1991). A perhaps more common way of characterizing the radiation intensity is to quote its value, often referred to as  $J_{912}$ , at  $\nu = \nu_{\text{HI}}$  or at wavelength 912 Å, in units of  $\text{ergsHz}^{-1}\text{s}^{-1}\text{cm}^{-2}\text{ster}^{-1}$ . The relation between  $J_{912}$  and  $J_{\text{HI}}$  depends on the spectrum. A good approximation for reasonable slopes of the spectrum right above  $\nu_{\text{HI}}$  ( $J_{\nu} \propto \nu^{-m}$  for  $m$  between 1 and 1.5) is  $J_{\text{HI}} = 0.7 J_{912} / 10^{-21}$ .

Second, we find that

$$T = T_0 (1 + \delta_b)^{\gamma-1}, \quad (19)$$

where  $T_0$  is not dependent on position, is a good approximation for overdensities of interest,  $\delta_b \lesssim 5$ , with a little flattening at the low end ( $\delta_b$  close to 0.1) for some reionization scenario. We will call this our equation of state. Note that this implies that the spatial dependence of  $T$  (and by extension  $X_{\text{HI}}$ ) is completely determined by that of  $\delta_b$ , which is true for UN shocked gas. Similar power law relation between the overdensity and the temperature can be seen in Fig. 2 of Weinberg et al. (1996) for low overdensity.

Third, both  $T_0$  and  $\gamma$  depend on the reionization history, the reasonable ranges being  $1.2 < \gamma < 1.7$  and  $3000 K < T_0 < 30000 K$  at  $\bar{z} = 3$ . Note that the range of  $\gamma$  includes the particular case of  $5/3$ , which holds if the gas evolves adiabatically.

Combining equations (19) and (17), it can be seen that the neutral hydrogen fraction is proportional to  $(1 + \delta_b)^{1-0.7(\gamma-1)}$ .

In conclusion to Sec. 3, we have outlined a procedure to use the Zel'dovich approximation, with appropriate initial smoothing, to produce a realization of  $\delta_b$  and  $v_{\text{pec}}$  as

a function of position and we have also shown how the relations between  $T$ ,  $X_{\text{HI}}$  and  $\delta_b$  can be obtained (eq. [19] and [17]). All of them enter into the calculation of the optical depth  $\tau$  (eq. [1] or [5]). We can compute  $e^{-\tau}$ , called the transmission, which is the ratio of the observed to the emitted intensities. Observationally, its measurement requires knowledge of the quasar emission spectrum. Moreover, one must carefully choose the range of frequencies to consider if one is to limit the source of absorption to that due to the Ly $\alpha$  transition. For a discussion of these issues, the reader is referred to Press, Rybicki and Schneider (1993). To produce a realistic spectrum, one should also add noise and convolve the transmission with a window function to mimic instrumental resolution. This is important for a detailed comparison between theories and observations, which we will defer to latter work. Our  $x$  space grid cells, depending on which particular simulation, have sizes ranging from 0.028 Mpc to 0.075 Mpc. Note that the true resolution in velocity space is not uniform because peculiar velocity varies from one place to another. Without peculiar velocity, the above grid cell sizes correspond to velocity cells of  $2.8 - 7.5 \text{ km s}^{-1}$ , for  $h = 0.5$  at  $\bar{z} = 3$  (eq. [3]). The true velocity resolution is probably a little worse than that. As a comparison, high quality Keck Telescope data have a Full-Width-Half-Maximum of about  $7 \text{ km s}^{-1}$  and signal to noise per pixel of the order of 30 or higher (Hu et al. 1995; Lu et al. 1996).

#### 4. The Peculiar Velocity: its Effects on Line Shapes and the Column Density Distribution

We show in this section that while the peculiar velocity plays an important role in determining the absorption profiles, its effect on the column density distribution is minor. The procedures to obtain the column density distribution are discussed first.

##### 4.1. Line Identification and the Column Density Distribution

Fig. 1 and Fig. 2 show the velocity, density and transmission ( $e^{-\tau}$ ) along two lines of sight for a  $\sigma_8 = 0.7$  CDM simulation, with  $h = 0.5$  (see Table 1). The significance of the dashed transmission profile will be explained in the next sub-section. The thermal and ionization parameters are described in the caption of Fig. 1. The truncation scale  $k_S$  (eq. [15]) is  $2.3 \text{ Mpc}^{-1}$ . The transfer function is taken from Ma (1996). We find that using the transfer function of Bardeen et al. (1986) makes almost no difference to the resulting column density distribution, for the range of column densities considered.

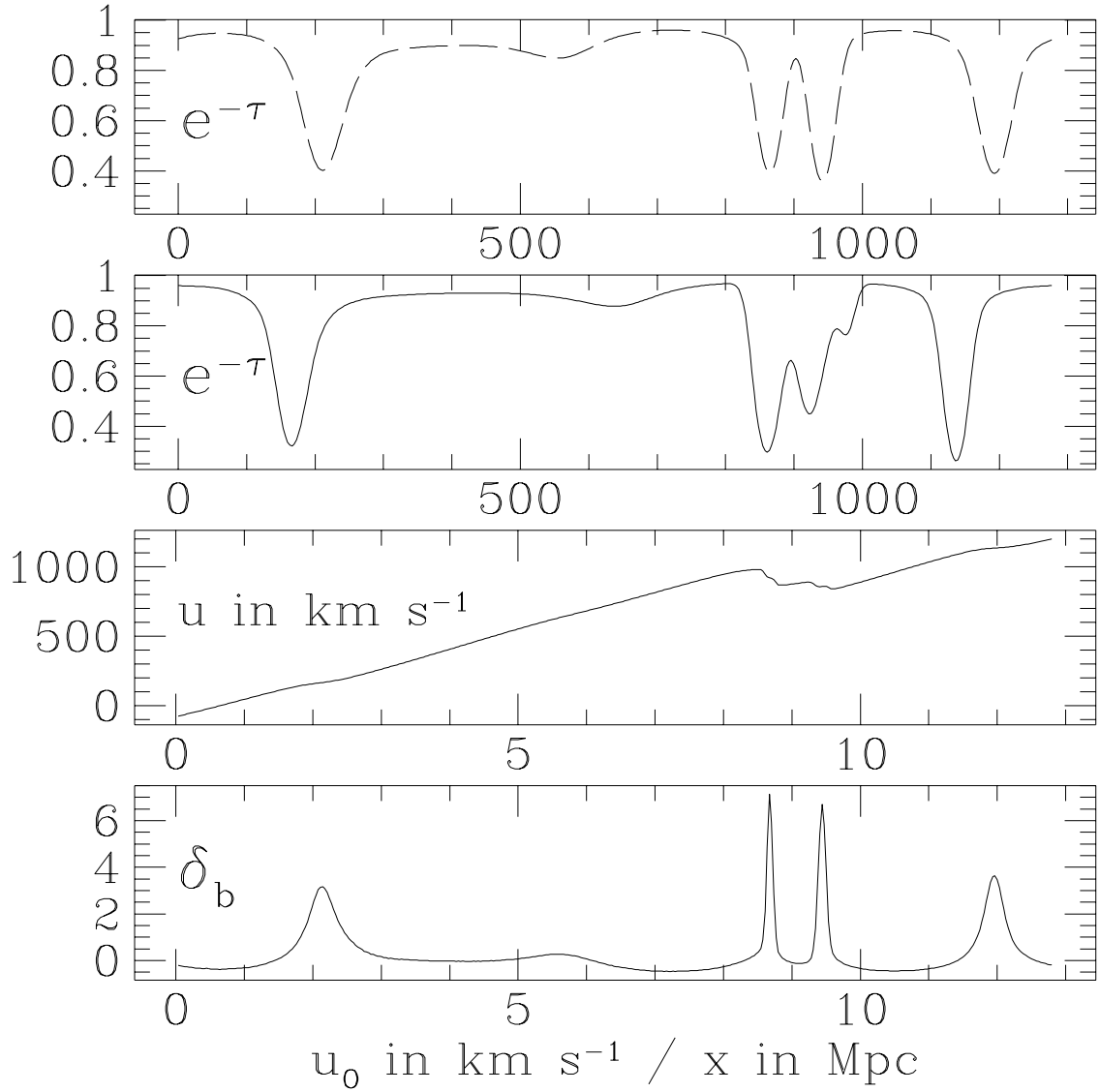


Fig. 1.— A line of sight through a  $\sigma_8 = 0.7$  CDM simulation (produced using the truncated Zel'dovich approximation) at  $\bar{z} = 3$ , with  $h = 0.5$ . The transfer function is taken from Ma (1996). Box size is 12.8 Mpc with a grid spacing of 0.032 Mpc. The parameters are  $\Omega_b h^2 = 0.0125$ ,  $J_{\text{HI}} = 0.5$ ,  $T_0 = 10^4 \text{ K}$ ,  $\gamma = 1.5$  and  $k_s = 2.3 \text{ Mpc}^{-1}$ . All distances are comoving. See Sec. 3 for definitions of the symbols. The abscissas for the lower two panels are the comoving distances along the line of sight in units of Mpc. The lower of the two panels is the profile of overdensity  $\delta_b$  (eq. [8]) and the upper one is the profile of velocity  $u$  (eq. [3]). The top two panels are both transmission profiles where  $\tau$  is the Ly $\alpha$  optical depth and the abscissas represent  $u_O$ , which is related to the observed frequency through equation (4). The profile with solid line is obtained using the full density and peculiar velocity fields. The profile with dashed line is obtained using the same density field but setting the peculiar velocity to zero everywhere (in which case,  $u$  becomes linear in  $x$ ).

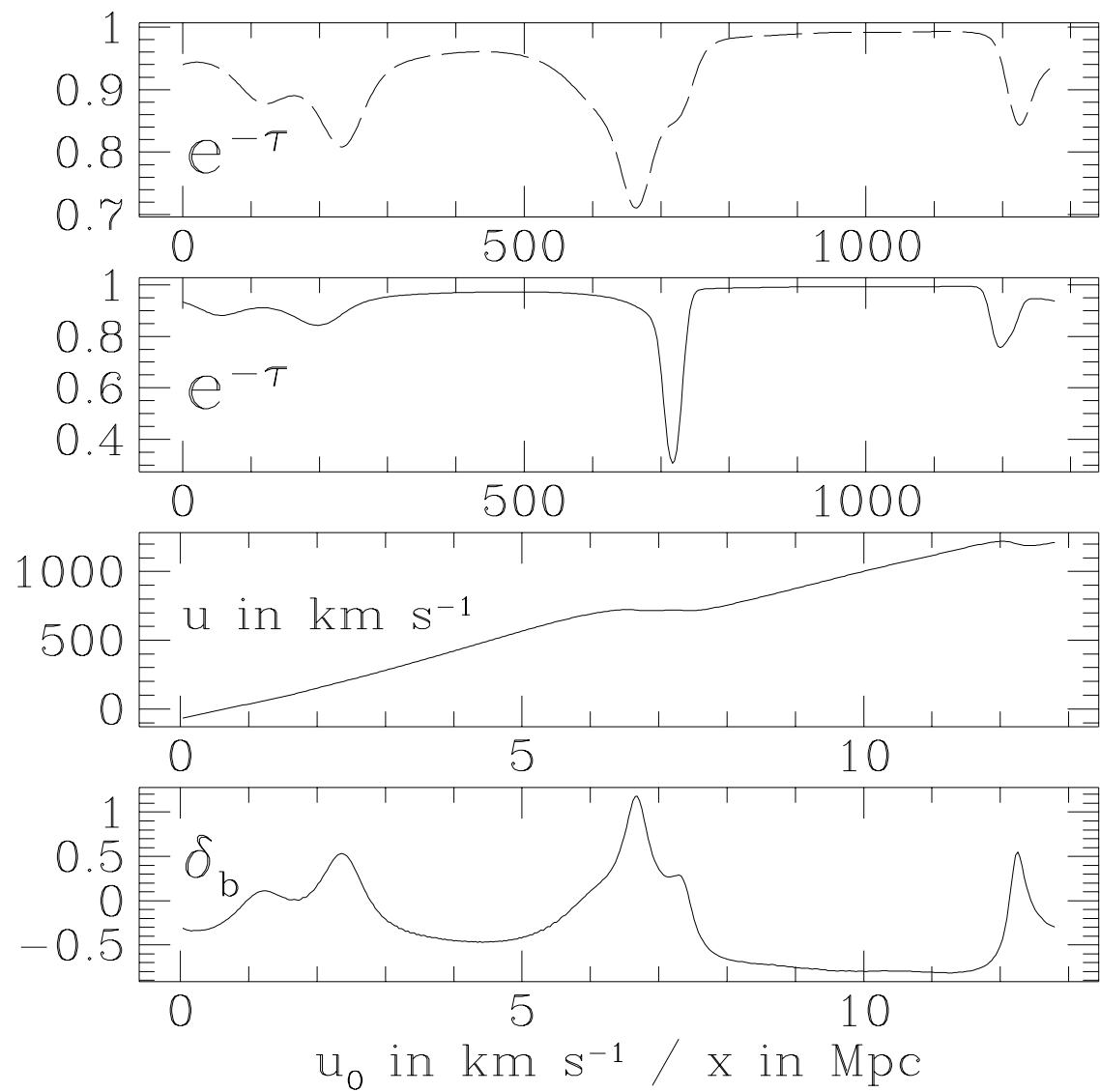


Fig. 2.— The same as in Fig. 1 but a different line of sight.

The first thing to note is that for the given parameters,

$$b \equiv \sqrt{\frac{2k_B T_0}{m_p}} = 13 \text{ kms}^{-1} (1 + \delta_b)^{1/4}. \quad (20)$$

This might seem to be too small because the observed lower limit of the  $b$ -value is about  $15 - 20 \text{ kms}^{-1}$  (Hu et al. 1995; Lu et al. 1996). There are two points to be made. First,  $T_0$  is the temperature of the gas at  $\delta_b = 0$ . The observed  $b$ -values might originate from regions at higher  $\delta_b$ . It is true though that the  $1/4$  power of  $1 + \delta_b$  does not help very much. Second, a distinction should be made between the observed  $b$ -value and the  $b$  defined above. The observed  $b$ -value is obtained by fitting the quasar spectrum with superpositions of the Voigt profiles. Each Voigt profile yields a column density and a  $b$ -value. All the density peaks that give rise to absorption troughs in Fig. 1 and Fig. 2 have velocity widths larger than or comparable to the small thermal width defined in equation (20). Therefore the narrow-maximum-limit (eq. [6]) does not apply and the absorption troughs do not exactly have the Voigt profile shapes. The  $b$ -value obtained from the best-fit Voigt profile of a given absorption trough does not necessarily correspond to the thermal width in equation (20). It should also be emphasized that the recent hydrodynamic simulations of the Ly $\alpha$  forest, which have been so successful in accounting for a lot of its observed properties, have similarly low temperatures (see for instance Weinberg et al. 1996 <sup>7</sup>).

One might wonder if there exists an alternative spectrum reduction method where the Voigt profile is not assumed to be the fundamental shape of absorption troughs, and for such a method, how the column density is assigned to each trough. The Voigt-profile-fitting-technique is nonetheless very important because it is how all existing observational data on the column density distribution are obtained.

An alternative line identification algorithm was proposed by Miralda-Escudé et al. (1995) and was also used by Hernquist et al. (1995). First a transmission ( $e^{-\tau}$ ) threshold ( $e^{-\tau}$ ) is chosen. Any part of the spectrum that is continuously below the threshold is identified as an absorption line. The column density associated with it is defined by

$$N_{\text{HI}} \equiv \frac{1}{\sigma_{\alpha 0}} \int_{\text{line}} \tau(u_O) \frac{du_O}{c}, \quad (21)$$

where  $\sigma_{\alpha 0}$  is defined after equation (5). The limits of integration are taken to be over the absorption line, i.e. where the transmission is continuously below the threshold. Note that

---

<sup>7</sup>Their output is at redshift of 2 and so naturally they have a lower temperature. In general, the temperature  $T_0$  is dependent on the reionization history of the universe: crudely speaking, the closer the epoch of reionization is to the epoch of observation ( $\bar{z} = 3$  in our case), the higher the temperature. Assuming reionization occurs before a redshift of 5, say, puts an upper bound on  $T_0$  (Hui and Gnedin 1996).

if the narrow-maximum-limit or the thin cloud assumption were to hold, equation (6) can be substituted into equation (21) to show that  $N_{\text{HI}}$  does correspond to  $\int n_{\text{HI}} dx / (1 + z)$ , assuming the threshold is high enough so that most of the Voigt profile is included in the definition of the absorption line.

Let us call the above procedure the Threshold-Algorithm. We show in Fig. 3 the column density distribution computed according to the algorithm (Crosses). The symbol  $d^2 N_{\text{Ly}\alpha} / dN_{\text{HI}} / dz$  denotes the number of absorption lines per unit column density per unit redshift. The reason for the chosen range of column densities will be given in Sec. 5. The transmission is chosen to be at the mean transmission of 0.89.

The Threshold-Algorithm has the tendency to underestimate the number of absorption lines compared to the Voigt-profile-fitting-technique. One reason is that it does not deblend. In other words, a given absorption line according to the Threshold-Algorithm may contain more than one minimum in transmission. Such an absorption line would be broken up to a few lines if the Voigt-profile-fitting-technique is employed. To demonstrate this effect, we modify the Threshold-Algorithm: for each (parent) absorption line identified, we break it up into individual components (children) where each component is bordered by local maxima in the transmission within the confines of the parent. The column density for each child component is defined similarly as in equation (21) and the limits of integration are taken to be the boundaries of each component. We will call it the Threshold-Deblending-Algorithm.

The resulting column density distribution is denoted by the square symbols in Fig. 3 for the transmission threshold of 0.89. One can see that indeed the number of lines of low column densities go up. We should emphasize however that the Threshold-Deblending-Algorithm cannot be used to analyze observational data without modifications because in real life, noise creates local transmission maxima within any parent absorption line.<sup>8</sup>

For now, the Threshold-Algorithm is adopted as a simple way to identify lines and assign column densities, which we will use to study the effects of the peculiar velocity on the column density distribution.

---

<sup>8</sup>In fact, numerical noise can also have the same effect. We check it by defining local maxima in two ways: local maxima over three cells and local maxima over five cells with the slope on either side of the maxima not changing signs. It turns out the resulting column density distributions are almost the same.

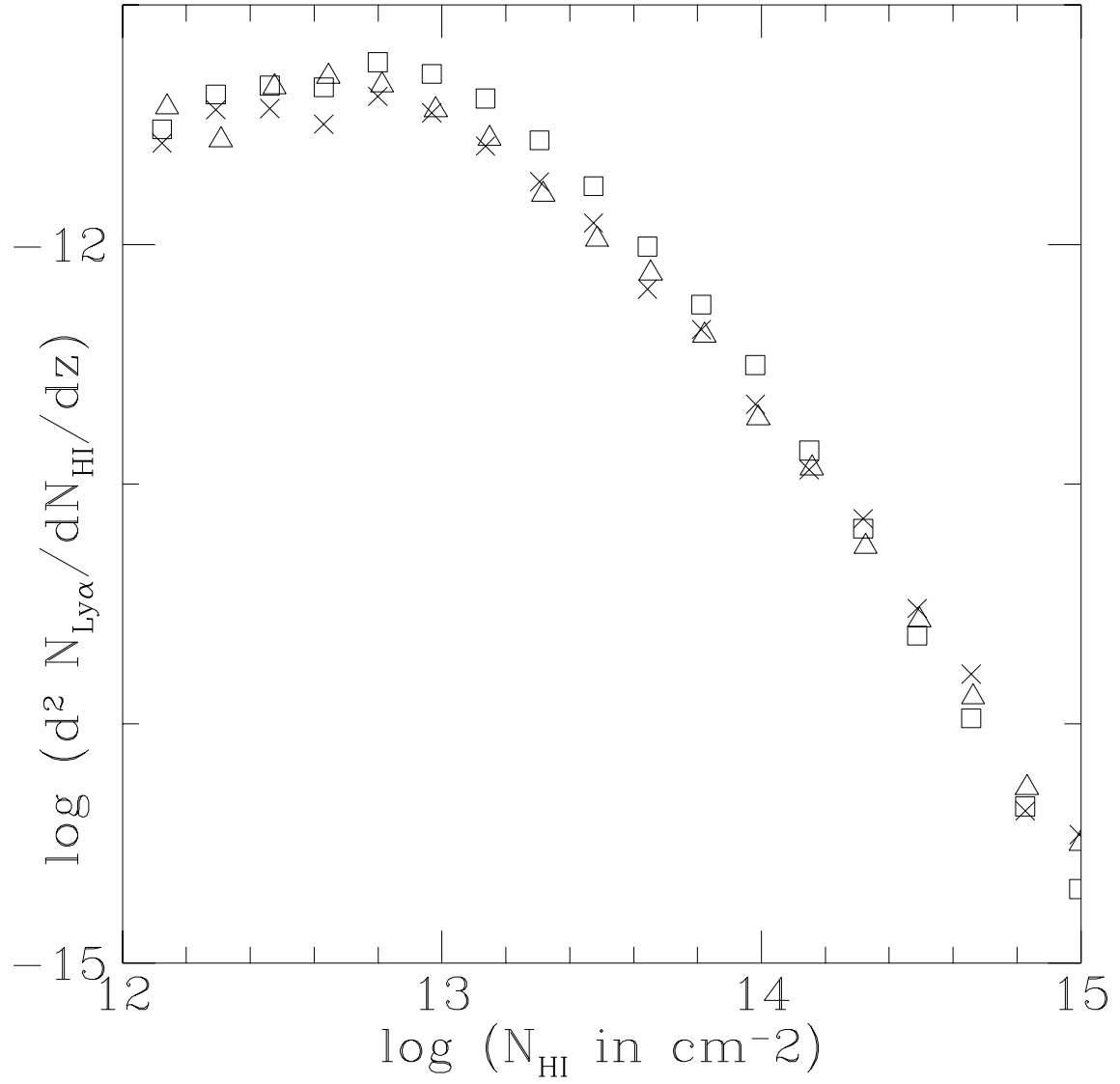


Fig. 3.— The column density distributions for the same model and parameters as those in Fig. 1. The quantity  $d^2N_{\text{Ly}\alpha}/dN_{\text{HI}}/dz$  has units of  $\text{cm}^2$ . Crosses represent the distribution obtained by applying the Threshold-Algorithm (threshold at 0.89, which is the mean transmission) to spectra generated using the density and peculiar velocity fields predicted by the truncated Zel'dovich approximation. Open triangles represent the same except that peculiar velocities are set to zero. Open squares are obtained by applying the Threshold-Deblending-Algorithm at the threshold of 0.89.

## 4.2. The Role of Peculiar Velocities

The following experiment is performed to investigate the importance of peculiar velocities. We generate absorption spectra and compute the column density distribution using the same density field as that used to produce the solid curves in Fig. 1, Fig. 2 and the squares and crosses in Fig. 3 but we set all peculiar velocities to zero.

Let us first examine some examples of the absorption spectra. The dashed curves in Fig. 1 and Fig. 2 are the resulting spectra after putting all peculiar velocities to zero.

A comparison of the dashed absorption spectrum with its solid counterpart in each figure shows that the peculiar velocities play an important role in determining the shapes of absorption lines. Without peculiar velocities, the shapes of absorption troughs mirror closely (perhaps a little thermally-broadened compared to) those of the density peaks while with nonzero peculiar velocities, the absorption troughs can have quite different shapes from the underlying density field. Peculiar velocities can add or erase structures. An example of the former can be found in the pair of density peaks around  $x = 9$  Mpc and their corresponding absorption profiles in Fig. 1. An example of the latter can be found in the density peak(s) around  $x = 7$  Mpc and the corresponding absorption trough(s) in Fig. 2.

Broadly speaking, the effects of peculiar velocities on absorption spectra fall into three categories. They are distinguished by the value of  $du/dx$  ( $u$  is defined in eq. [3]). First, there are regions in space where the peculiar velocity gradient is small so that  $du/dx$  is almost equal to its Hubble value  $\bar{H}/(1 + \bar{z})$  (eq. [3]). An example is the density peak around  $x = 2.2$  Mpc in Fig. 2. The peculiar velocity shifts the position of the associated absorption trough but does not affect its shape.

Second, there are places where the peculiar velocity gradient is opposite in sign and comparable in magnitude to  $\bar{H}/(1 + \bar{z})$ , in which case  $|du/dx|$  becomes very small. Suppose also that  $|d^2u/dx^2|$  is small. The implication is that a small range in  $u$  corresponds to a relatively large range in  $x$ . See for instance the density peak(s) around  $x = 7$  Mpc in Fig. 2, which is a really broad structure in  $x$  space but is relatively narrow in  $u$  space if peculiar velocities are not put to zero. The small  $|du/dx|$  or the converging peculiar velocity flow around it helps to produce a narrow absorption trough (second panel from the top in Fig. 2). Contrast it with the corresponding absorption feature in the top panel of the same figure, where peculiar velocities are set to zero. The limiting case where  $|du/dx|$  exactly vanishes is called a velocity caustic (McGill 1990).

Third, there are regions where the peculiar velocity gradient dominates in such a way that  $du/dx$  is negative and  $|du/dx|$  is not small. An example can be found around the pair of density peaks at  $x = 9$  Mpc in Fig. 1. This is where multiple-streaming occurs. A given

range in  $u$  corresponds to disjoint pieces in  $x$  space. As a result, the shapes of the associated absorption troughs are significantly different from those of the underlying density peaks.

The three categories can be shown to correspond to the three evolutionary stages of a pancake collapsing along the line of sight (McGill 1990). Restricting equations (11) and (12) to one dimension and putting it into equation (3), one obtains:

$$\frac{du}{dx} = \dot{a} \left( 1 + 2a \frac{d^2\psi}{dq^2} \right) \left( 1 + a \frac{d^2\psi}{dq^2} \right)^{-1}, \quad (22)$$

where we have assumed a universe of critical matter density so that  $D_+ = a$ . Restricting equation (12) to one dimension, it can also be shown that

$$1 + \delta_b = \left( 1 + a \frac{d^2\psi}{dq^2} \right)^{-1}, \quad (23)$$

where we have replaced  $\delta_{\text{DM}}$  by  $\delta_b$  assuming the appropriate initial smoothing has been carried out as indicated in Sec. 3.1. As  $a$  grows, it can be seen that  $du/dx$  goes through the three different regimes outlined above. At the velocity caustic where  $du/dx = 0$ , it can be shown that  $\delta_b = 1$  (McGill 1990). This conclusion does not hold in general of course because pancakes can collapse in directions different from the line of sight. But it is true that velocity caustics are often found in regions of slight overdensities.

In principle, at a velocity caustic, an absorption line can arise even without any variation in the density field at all (eq. [5]). In practice, one expects that converging peculiar velocity flows are accompanied by density peaks. This is consistent with the few examples we have seen.

Next, we consider how the column density distribution changes when the same density field is used but all the peculiar velocities are put to zero. This is shown in Fig. 3.

The mean transmission of the analysis with zero peculiar velocities differ from the mean transmission of the full analysis by less than a percent. It is used as the transmission threshold in the line identification procedure for both analyzes. The resulting column density distributions are very similar.

Hence, the peculiar velocity plays a relatively minor role in determining the column density distribution. It changes the shapes of absorption troughs without altering the overall number of lines and their column densities. This serves to motivate an approximation we will introduce in the next section.

A final note on velocity caustics. The reader might worry that at a velocity caustic, the optical depth may diverge while it is clear from equation (1) that for a finite number

density of neutral hydrogen, the optical depth should always be a finite quantity. The resolution is that close to a velocity caustic at  $u = u_c$ ,  $du/dx$  goes like  $(u - u_c)^{1/2}$  (provided the second derivative of  $u$  with respect to  $x$  is nonzero, otherwise it will be  $(u - u_c)^{2/3}$  if the third derivative does not vanish and so on, by simple Taylor series expansion; see Shandarin and Zel'dovich 1989 for a similar analysis applied to real caustics as opposed to velocity caustics; orbit-crossing occurs in the former but not the later). So under the integration in equation (5), the optical depth remains finite. We note also that because of the singular nature of  $(du/dx)^{-1}$  around  $u = u_c$ , the derivation leading to equation (7) breaks down at a velocity caustic.

## 5. The Statistics of Density Peaks

In this section we explore a simple approximation in which each density peak in  $x$  space is identified with an absorption line. This is motivated by the fact that peculiar velocities do not play a major role in determining the column density distribution and that each maximum in density corresponds to a minimum in the absorption spectrum if the peculiar velocities are set to zero and if the maximum in density is separated from other maxima by a distance larger than that given by the thermal broadening width.

To calculate  $d^2N_{\text{Ly}\alpha}/dN_{\text{HI}}/dz$ , we relate  $dz$  and  $dx$  by ignoring peculiar velocities:  $dz = c^{-1}\bar{H}dx$ . Hence

$$\frac{d^2N_{\text{Ly}\alpha}}{dN_{\text{HI}}dz} = \frac{d^2N_{\text{pk}}}{dN_{\text{HI}}dx} \frac{c}{\bar{H}}, \quad (24)$$

where  $dN_{\text{pk}}/dN_{\text{HI}}/dx$  is the average comoving number density of density peaks along a random line of sight per unit column density,  $\bar{H}$  is the Hubble constant at the redshift of interest.

For each density peak, we need a simple prescription for assigning a column density. To that end, we do the following expansion around each density maximum:

$$\ln[n_{\text{HI}}(x)] = \ln[n_{\text{HI}}(x_{\text{pk}})] + \frac{1}{2} \left. \frac{d^2 \ln[n_{\text{HI}}]}{dx^2} \right|_{x=x_{\text{pk}}} (x - x_{\text{pk}})^2. \quad (25)$$

It is a straightforward Taylor expansion around the position of the peak  $x_{\text{pk}}$ . The second derivative in the last term is negative. The rationale behind expanding  $\ln[n_{\text{HI}}]$  rather than  $n_{\text{HI}}$  itself is that  $n_{\text{HI}}$  is supposed to fall off quickly far away from the peak (until, of course, another peak is encountered). In other words, the above expansion implies that  $n_{\text{HI}}$  has a Gaussian fall-off (instead of a power-law one if  $n_{\text{HI}}$  itself were Taylor expanded). In a sense, this is close in spirit to the Voigt-profile-fitting-technique. Suppose the

broad-maximum-limit (eq. [7]) holds so that the local optical depth is simply proportional to the number density of neutral hydrogen if one ignores peculiar velocities. Then, fitting a minimum in optical depth with the Voigt or thermal profile (eq. [5]) is equivalent to fitting the corresponding neutral hydrogen density peak with a Gaussian.

We then assign the following column density to the density peak:

$$N_{\text{HI}} = \int_{\text{pk}} \frac{dx}{1 + \bar{z}} n_{\text{HI}}(x) = n_{\text{HI}}(1 + \bar{z})^{-1} \sqrt{2\pi \left( \frac{-d^2 \ln[n_{\text{HI}}]}{dx^2} \right)^{-1}} \Big|_{x=x_{\text{pk}}} \quad (26)$$

where equation (25) has been used and where  $\int_{\text{pk}}$  denotes integration around the peak until it decays sufficiently. All  $x$  dependent terms on the right hand side are evaluated at  $x = x_{\text{pk}}$ . The above equation is also derived by the authors in a separate paper, using the Stationary Phase Method (Gnedin and Hui 1996).

Using equations (17) and (19), the above can be rewritten as:

$$N_{\text{HI}} = 1.63 \times 10^{13} \text{ cm}^{-2} \left( \frac{T_0}{10^4 K} \right)^{-0.7} \left( \frac{\Omega_b h^2}{0.0125} \right)^2 \left( \frac{J_{\text{HI}}}{0.5} \right)^{-1} \left( \frac{1 + \bar{z}}{4} \right)^5 \left( \frac{2 - 0.7(\gamma - 1)}{1.65} \right)^{-0.5} A \quad (27)$$

where  $A$  is defined by

$$A \equiv (1 + \delta_b)^{2-0.7(\gamma-1)} \left( \frac{-d^2 \ln[1 + \delta_b]}{dx^2} \right)^{-\frac{1}{2}} \Big|_{x=x_{\text{pk}}} , \quad (28)$$

with  $x$  being measured in Mpc.

We will refer to our method as the Density-Peak-Ansatz. It consists of two parts: 1. associate each density peak in  $x$  space with an absorption line; 2. assign a column density to each density peak according to equation (27).<sup>9</sup>

Making use of equations (24) and (27), the column density distribution can be written as

$$\frac{d^2 N_{\text{Ly}\alpha}}{dN_{\text{HI}} dz} = 6.25 \times 10^{-14} \text{ cm}^2 \left( \frac{T_0}{10^4 K} \right)^{0.7} \left( \frac{\Omega_b h^2}{0.0125} \right)^{-2} \left( \frac{J_{\text{HI}}}{0.5} \right) \left( \frac{1 + \bar{z}}{4} \right)^{-5} \left[ \frac{2 - 0.7(\gamma - 1)}{1.65} \right]^{0.5} \frac{c}{H} \frac{d^2 N_{\text{pk}}}{dA dx} , \quad (29)$$

---

<sup>9</sup>Strictly speaking, care should be taken not to count peaks that are separated in velocity space by distance much less than the thermal width as contributing to more than one absorption line. We will address this later in the section.

where  $x$  is in units of Mpc. The computation of the last factor  $d^2N_{\text{pk}}/dA/dx$  involves counting the number density of peaks in  $x$  space having the quantity  $A$  within the range  $dA$ .

Let us define  $\xi \equiv \ln[1 + \delta_b]$ . Suppose one is given  $P(\xi, \xi', \xi'')d\xi d\xi' d\xi''$  which is the probability that  $\xi$  and its first and second derivatives with respect to  $x$  fall in the specified ranges at a point. Then,

$$\frac{dN_{\text{pk}}}{dx} = \int_{-\infty}^{\infty} d\xi \int_{-\infty}^0 d\xi'' |\xi''| P(\xi, \xi' = 0, \xi''), \quad (30)$$

where  $\frac{dN_{\text{pk}}}{dx}$  is the integral of  $\frac{d^2N_{\text{pk}}}{dA dx}$  over all  $A$  (Bardeen et al. 1986).

By a change of variable and a differentiation and making use of equation (28), one can obtain

$$\frac{d^2N_{\text{pk}}}{dA dx} = \frac{1}{[2 - 0.7(\gamma - 1)]A} \int_{-\infty}^0 d\xi'' |\xi''| P(\xi, \xi' = 0, \xi'') \quad (31)$$

where  $\xi$  should be expressed in terms of  $\xi''$  and  $A$  using equation (28).

Note that the above two equations are completely general and no assumption about the Gaussianity of the underlying fields has been made. The hard part is of course to come up with the probability function  $P$ . The one point probability distribution of just  $\xi$  or density has been calculated for the Zel'dovich approximation (Kofman et al. 1994). We find the one point joint-probability distribution of density and its first and second derivatives along a line of sight difficult to calculate analytically for the Zel'dovich approximation. A numerical approach is adopted in this paper and the number of peaks is counted along random lines of sight in actual three-dimensional realizations. In a separate paper, we discuss an analytical calculation based upon not the Zel'dovich approximation but the lognormal approximation, where  $\xi$  is assumed to be a Gaussian random field (Gnedin and Hui 1996). A comparison between the two will be made.

We test the Density-Peak-Ansatz in two different ways. First, we make a scatter plot of the column density obtained using the Threshold-Deblending-Algorithm versus the column density obtained by searching for the maximum density peak that contributes to each absorption line identified using the threshold method and then applying equation (27). The result is shown in Fig. 4. It shows that while the agreement is far from perfect, the column densities assigned using the Density-Peak-Ansatz and using the Threshold-Algorithm are broadly consistent.

The important question, however, is whether the Density-Peak-Ansatz, coupled with the Zel'dovich approximation with appropriate initial smoothing, gives the correct number of absorption lines as a function of column density. We compare the column density

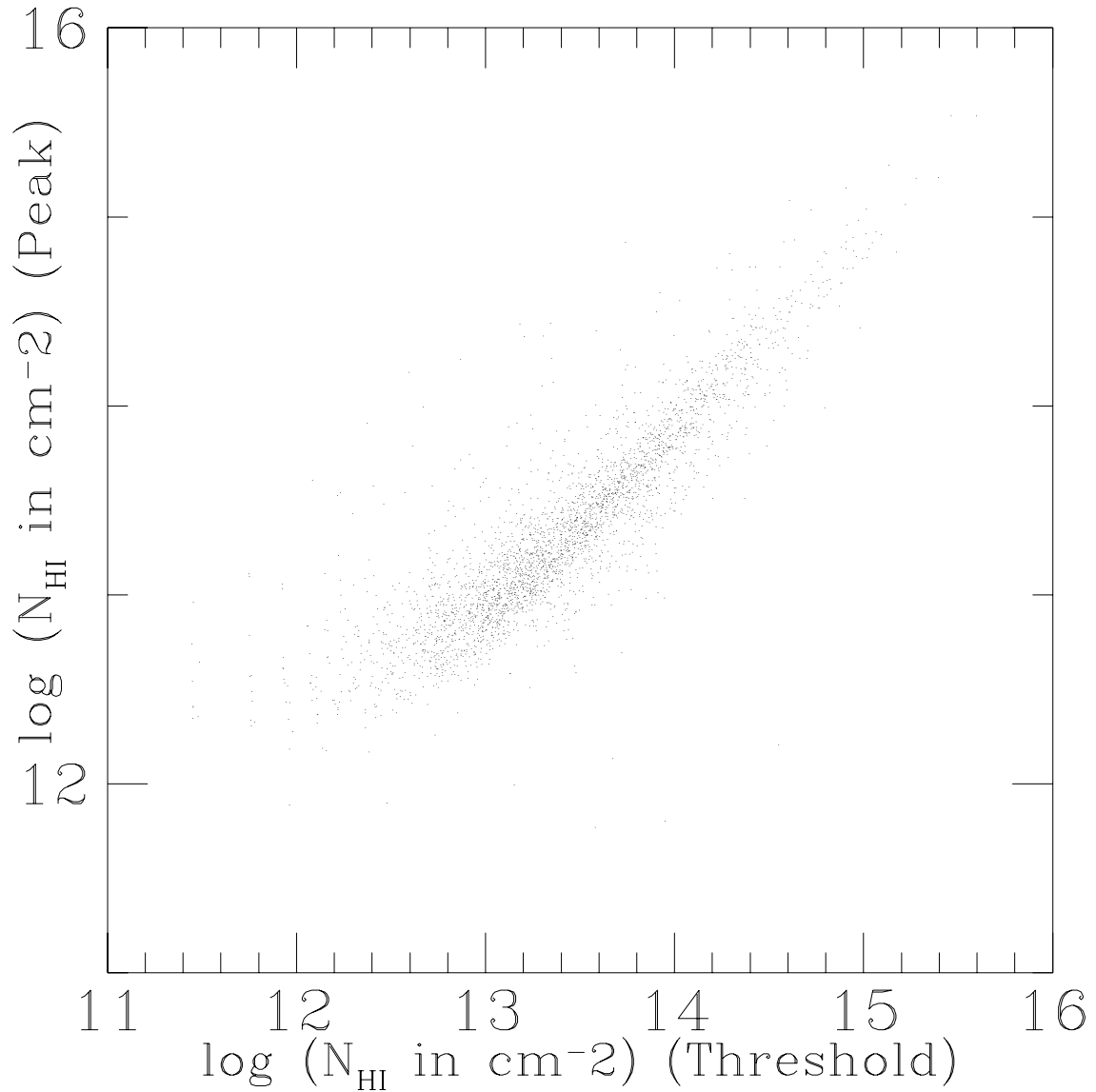


Fig. 4.— Same parameters as in Fig. 1. The column densities computed using two different methods are plotted against each other. First, we identify absorption lines by the Threshold-Deblending-Algorithm using a transmission threshold of 0.89 and assign column densities according to equation (21), which are plotted as the abscissas. We then take each absorption line identified using the Threshold-Deblending-Algorithm and search for the corresponding maximum in  $\delta_b$  and apply equation (27) to assign a second set of column densities, which are plotted as the ordinates.

distribution obtained using our approximate methods against that obtained by applying the Voigt-profile-fitting-technique to synthetic spectra from a full hydrodynamic simulation (see Zhang et al. 1996 for details). This is done in Fig. 5.<sup>10</sup> We also put in the same figure the column density distribution obtained using the Threshold-Algorithm, coupled with the Zel'dovich approximation. The predictions of the lognormal approximation are shown as well for comparison.

The level of agreement between the exact hydrodynamic computation and our calculation based on the Density-Peak-Ansatz coupled with the Zel'dovich approximation is encouraging. Two sets of points are shown for our approximate calculation using the Density-Peak-Ansatz, one (open triangles) with exactly the same box size and grid spacing as the hydrodynamic simulation and the other (open squares) with larger box size and smaller grid spacing. They both agree very well with the exact computation. We will explore the effects of changing the resolution in the next sub-section. A third set of points (crosses) shows that the Threshold-Algorithm described in Sec. 4.2 underestimates the number of lines at low column densities.

We also show in Fig. 5 two sets of curves based on the lognormal approximation but using the same Density-Peak-Ansatz (see Gnedin and Hui 1996). One of them has the same amount of initial smoothing as that of the truncated Zel'dovich approximation and the other has less smoothing so as to match the final (not linear) rms density fluctuation of the Zel'dovich computation. Both underestimates the number of lines at low column densities. The lognormal approximation tends to predict too much flattening of the column density distribution at low column densities. In general the lognormal approximation tends to give column density distribution that deviate quite significantly from power-law unless a very small smoothing length  $k_S^{-1}$  is chosen. (From the figure, it might appear that the lognormal approximation gives more lines than the Zel'dovich approximation at the very low column densities but it is really a resolution effect: see the next sub-section.)

The reader might have noticed that we have included in Fig. 5 a wider range of column densities than is warranted by the nature of our approximations. For instance, objects with column densities higher than  $10^{16} \text{ cm}^{-2}$  are almost certainly highly nonlinear and we do not expect the truncated Zel'dovich approximation to work well in this regime. For the low column densities, the finite resolution should cause us to underestimate the number of absorption lines. In the next sub-section, we give quantitative estimates of the range

---

<sup>10</sup>Note that the value of  $\gamma$  given in the caption of Fig. 5 is obtained directly from the hydrodynamic simulation. The temperature-density relation is not an exact power law but is well approximated by one for the relevant range of densities.

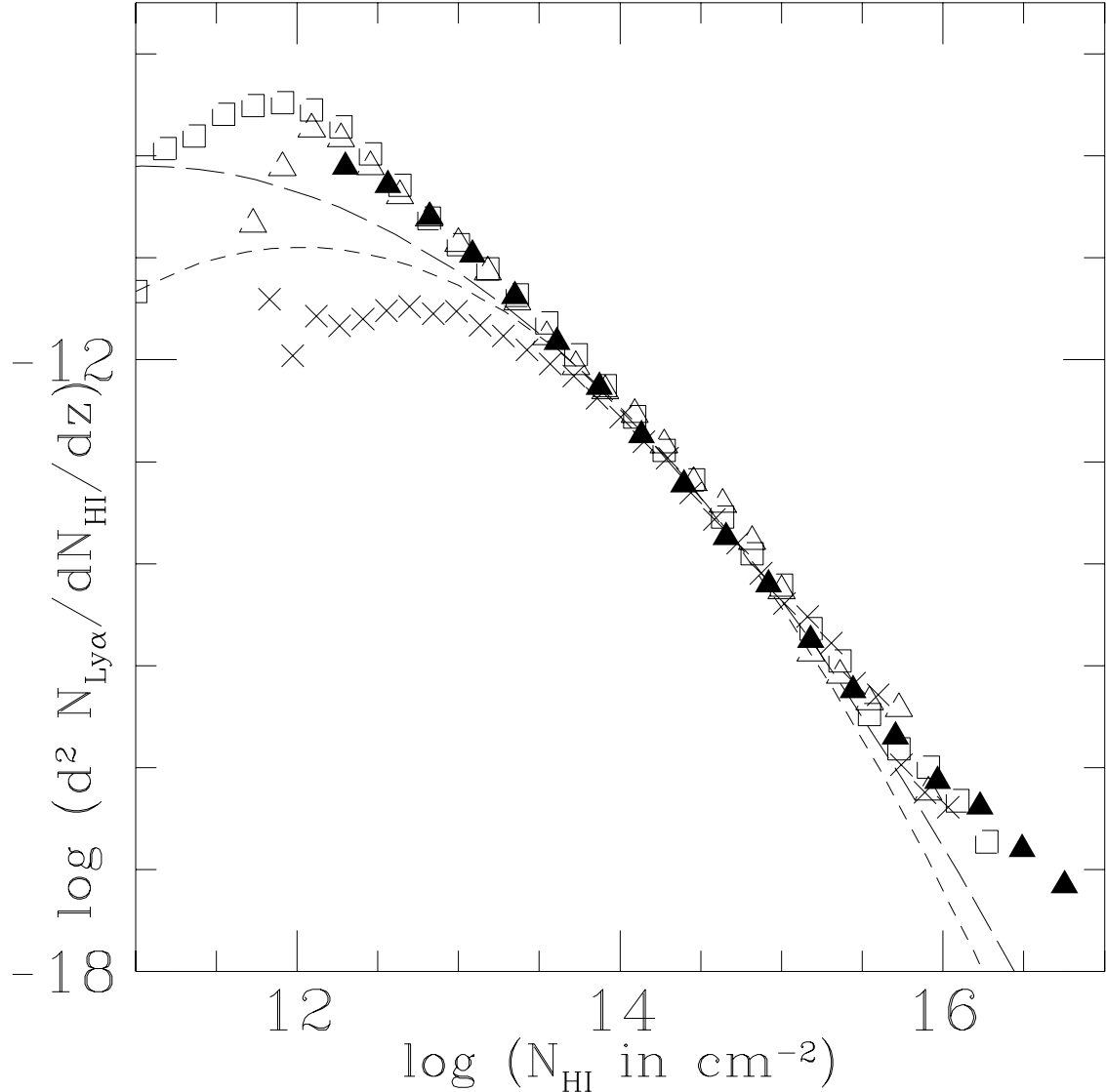


Fig. 5.— The model is  $\sigma_8 = 0.7$  CDM at  $\bar{z} = 3$  with  $h = 0.5$ ,  $\Omega_b = 0.06$ ,  $J_{\text{HI}} = 0.325$ ,  $T_0 = 10^4 K$  and  $\gamma = 1.45$ . Solid triangles represent the distribution obtained by applying the Voigt-profile-fitting-technique to synthetic spectra from a full hydrodynamic simulation (Zhang et al. 1996) with box size of 9.6 Mpc comoving and grid spacing of 0.075 Mpc. Open triangles are the predictions of the Density-Peak-Ansatz coupled with the truncated ( $k_S = 2.3 \text{ Mpc}^{-1}$ ) Zel'dovich approximation using the same box size and grid-spacing. Open squares and crosses are the results of applying the Density-Peak-Ansatz and the Threshold-Algorithm (transmission threshold at 0.83, the mean transmission) respectively to the output of the same truncated ( $k_S = 2.3 \text{ Mpc}^{-1}$ ) Zel'dovich approximation with box size of 12.8 Mpc and grid spacing of 0.05 Mpc. The short-dashed and long-dashed curves are the predictions of the Density-Peak-Ansatz coupled with the lognormal approximation, the former with  $k_S = 2.3 \text{ Mpc}^{-1}$  and the latter with the smoothing scale chosen so that the final (not linear) rms density fluctuation matches that of the Zel'dovich approximation ( $k_S = 3.6 \text{ Mpc}^{-1}$ ).

of column densities within which the Density-Peak-Ansatz, used in conjunction with the truncated Zel'dovich approximation, can be counted upon to give reliable column density distributions.

We will also discuss two different ways of defining a density peak in the next sub-section: local maxima over three cells or local maxima over five cells with the slope on either side of the maxima not changing signs. The three-cell criterion is used in Fig. 5. One expects however that some of the three-cell peaks are not real but merely artifacts of numerical noise, especially those with low column densities. The five-cell criterion, on the other hand, probably fails to include some narrow peaks which are real. We will see that the two different criteria give almost identical results above a certain column density.

One aspect of the Density-Peak-Ansatz we have glossed over is that two density peaks that are separated by a distance in velocity space much less than the thermal width should be counted as contributing to not two but one absorption line. A more sophisticated approach would be to group together such density peaks and use the sum of their column densities as the column density of one single absorption line. We find that for the the range of validity discussed in the following sub-section, it makes little difference. It is conceivable, however, that this effect cannot be ignored for simulations with higher resolution than what we have.

### 5.1. The Range of Validity

For the computation presented in Fig. 5, the column density (given by the Density-Peak-Ansatz) above which the mean  $\delta_b$  exceeds 5 is about  $10^{14.1} \text{ cm}^{-2}$ . For the parameters listed in the caption of Fig. 5,  $N_{\text{HI}} = 3.6 \times 10^{13} \text{ A cm}^{-2}$  (eq. [27]). We therefore take  $A = 3.5$  as an upper limit beyond which we cannot expect our approximations to be reliable.

Note that according to Fig. 5, comparing with the hydrodynamic simulation data, the Density-Peak-Ansatz coupled with the truncated Zel'dovich approximation, seems to give reliable number density of absorption lines even for column densities higher than  $10^{14.1} \text{ cm}^{-2}$ . The level of agreement at such high column densities (and by extension, such high  $\delta_b$ ) is surprising. We will take the conservative approach and adopt the  $A = 3.5$  upper limit.

To determine the column density below which finite resolution results in an underestimate of the number of absorption lines, we perform a simulation using the truncated Zel'dovich approximation with the same parameters as the open squares in Fig. 5 but higher resolution: same box size of 12.8 Mpc but smaller grid spacing of 0.0284 Mpc. A comparison of the resulting column density distributions is made in Fig. 6.

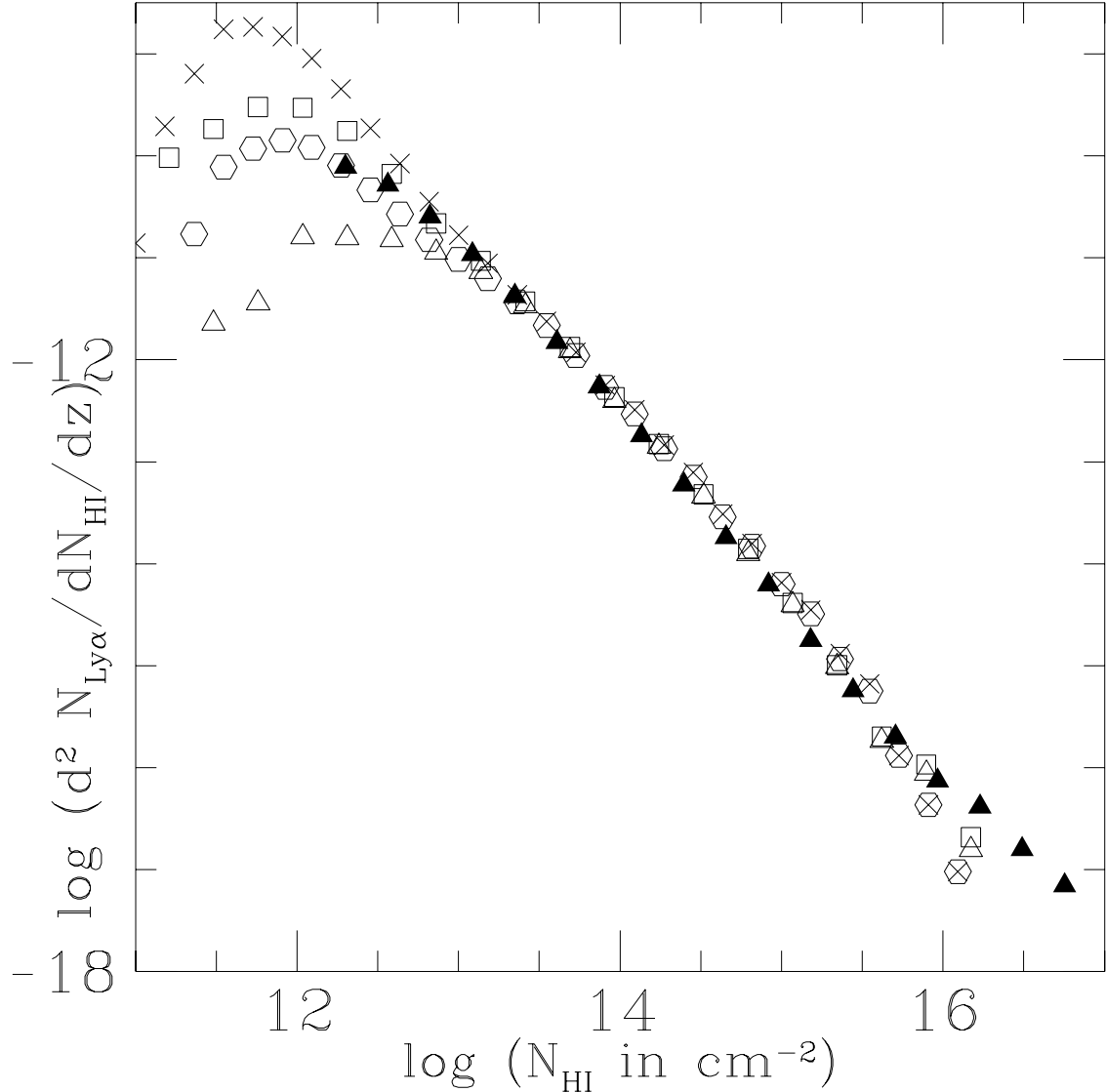


Fig. 6.— The solid triangles are same as those in Fig. 5, representing the column density distribution obtained by applying the Voigt-profile-fitting-technique to synthetic spectra from a full hydrodynamic simulation. The rest of the points represent the column density distributions obtained using the Density-Peak-Anätz in conjunction with the truncated Zel'dovich approximation for two simulations of different resolutions but the same cosmological, thermal and ionization parameters as in Fig. 5. The open squares and open triangles represent the distributions of a simulation with box size of 12.8 Mpc and grid spacing of 0.05 Mpc (all distances quoted are comoving). The open squares here are the same as those in Fig. 5 where each maximum over three cells is identified as a peak. The open triangles are the result of a different definition of peaks: a local maximum over five cells with the density slope on each side of the maximum not changing signs. Similarly, the crosses and open hexagons are the distributions for a simulation of box size 12.8 Mpc and grid spacing 0.0284 Mpc, using the three-cell and five-cell definition of peaks respectively.

Note that we have included two definitions of density peaks (three-cell and five-cell). For each simulation, the true column density distribution is probably somewhere between the two in the places they differ.

We take the low column density cut-off to be  $10^{12.8} \text{ cm}^{-2}$  for the lower resolution simulation (box size of 12.8 Mpc, with grid spacing of 0.05 Mpc) using the three-cell definition of peaks. It can be seen that the higher resolution simulation differs from the lower one only at column densities less than roughly this cut-off value. Moreover, above this column density, the three-cell and five-cell criteria give almost identical results.

The parameters in the simulations in Fig. 6 are such that  $N_{\text{HI}} = 3.6 \times 10^{13} A \text{ cm}^{-2}$  (eq. [27]). Hence the above column density cut-off implies a lower limit of 0.18 for  $A$ . From now on, we will use the three-cell definition of density peaks.

In the following section, we systematically investigate how the column density distribution depends on the cosmological parameters and properties of the intergalactic medium. All the simulations presented in the next two sections have the same resolution and box size,  $256^3$  grid points with grid spacing of 0.05 Mpc. For each of them, we will only plot the part of the column density distribution that falls within the limits of  $0.18 < A < 3.5$ . The column densities these limits correspond to depend on the properties of the intergalactic medium and the redshift (eq. [27]). Note how our conservative limits for  $A$  greatly reduce the range of column densities we can examine but within these limits, we can be reasonably confident that the truncated Zel'dovich approximation together with the Density-Peak-Ansatz should yield accurate predictions for the column density distribution.

## 6. The Column Density Distribution of the CDM models: Dependence on the Ionization Flux, Temperature, Equation of state and Cosmological Parameters

The Cold Dark Matter (CDM) models are used to study the influence of the cosmological parameters and properties of the intergalactic medium on the column density distribution. The tools we use to calculate the column density distributions are the truncated Zel'dovich approximation and the Density-Peak-Ansatz.

All CDM models discussed here have  $\Omega_0 = 1$ ,  $h = 0.5$  and are dark matter dominated. We use the Ma (1996) CDM transfer function. More detailed discussions of the simulations and the low and high column density cut-offs can be found at the end of Sec. 5.1. Table 1 contains a summary of all the CDM models discussed in this paper.

### 6.1. Dependence on Overall Temperature, Ionization Flux and Baryon Density

Let us first consider the CDM model with  $\sigma_8$  and the spectral index  $n$  being fixed at 0.7 and 1 respectively. Let us also hold the equation of state at  $T \propto (1 + \delta_b)^{0.5}$ . As is shown in equation (27), the column density of a density peak with a given  $\delta_b$  (overdensity) is proportional to the following combination of parameters:

$$F \equiv \left( \frac{T_0}{10^4 K} \right)^{-0.7} \left( \frac{\Omega_b h^2}{0.0125} \right)^2 \left( \frac{J_{\text{HI}}}{0.5} \right)^{-1}. \quad (32)$$

Hence, by equation (29), if  $F$  is rescaled by a certain factor (by changing  $T_0$ ,  $\Omega_b$  or  $J_{\text{HI}}$  or their combinations), the number of absorption lines is also changed by the same factor at an appropriately rescaled column density.

Suppose  $F$  is rescaled to  $F'$  such that  $F' = rF$ , then

$$\frac{d^2 N'_{\text{Ly}\alpha}}{dN'_{\text{HI}} dz} \bigg|_{N'_{\text{HI}} = rN_{\text{HI}}} = \frac{1}{r} \frac{d^2 N_{\text{Ly}\alpha}}{dN_{\text{HI}} dz} \bigg|_{N_{\text{HI}}}. \quad (33)$$

It implies that if the column density distribution is a pure power law, then in a log-log plot of the number of absorption lines per unit column density per unit redshift versus column density, the straight line would simply be shifted to the right or left (or up/down) by rescaling. In reality, the column density distribution only approximately obeys a power law and so there should be a slight change of slope at any given column density as a result of rescaling.

The effects of rescaling can be seen clearly in Fig. 7, where  $F$  is allowed to take the values 0.25, 1 and 5. Keeping  $\Omega_b h^2 = 0.0125$  and  $J_{\text{HI}} = 0.5$ , it corresponds to changing  $T_0$  from about 72000 K to 1000 K. Alternatively, keeping  $T_0$  and  $\Omega_b h^2$  fixed at their canonical values (as shown in eq. [32]), it corresponds to allowing  $J_{\text{HI}}$  to vary between 2 and 0.1. See Hui and Gnedin (1996) for a discussion of the dependence of  $T_0$  on reionization history.  $T_0$  is expected to fall within the range quoted above.

The conventional value of  $\Omega_b h^2 = 0.0125$  has been challenged by recent measurements of light element abundance in high redshift absorption systems. Tytler and Burles (1996) obtain a value of 0.024, which for  $T_0 = 10^4$  K and  $J_{\text{HI}} = 0.5$ , implies  $F = 3.686$ , well within the range of  $F$  plotted in Fig. 7. The analysis of Hogan and Rutgers (1996), on the other hand, favors the value 0.006, which means  $F = 0.23$  for the same values of  $T$  and  $J_{\text{HI}}$ . The lowest set of points in Fig. 7 has to be lowered further to accommodate this value of the baryon density.

The observational data are taken from Hu et al. (1995), measured at about redshift of 3 and corrected for incompleteness.

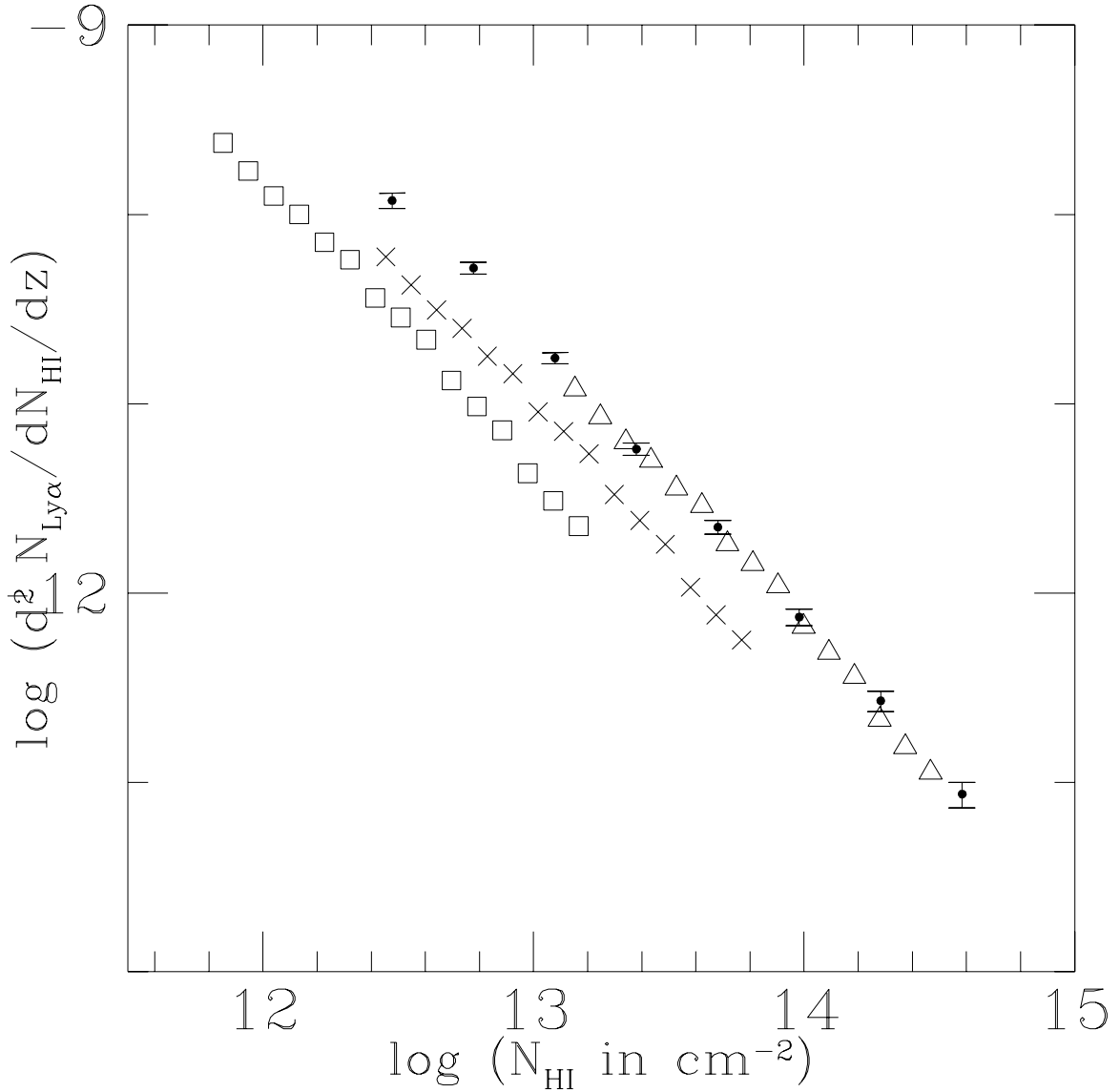


Fig. 7.— The column density distribution of the  $\sigma_8 = 0.7$  CDM model with no tilt (CDM1 in Table 1), obtained using the Density-Peak-Ansatz and the truncated Zel'dovich approximation ( $k_S = 2.3 \text{ Mpc}^{-1}$ ). The redshift is  $\bar{z} = 3$ . Box size is 12.8 Mpc with grid spacing of 0.05 Mpc. Open squares:  $F = 0.25$  (eq. [32]). Crosses:  $F = 1$ . Open triangles:  $F = 5$ . All of them have the equation of state described by  $\gamma = 1.5$  (eq. [19]). The points with error bars are the observational data at about  $z = 3$  which have been corrected for incompleteness, taken from Hu et al. (1995).

We note in passing that strictly speaking, altering  $\Omega_b$ , in addition to rescaling the number of absorption lines as discussed above, also changes the transfer function in a non-trivial way. But the effect is very small for models in which the dark matter (non-baryons) dominate. In fact, using the BBKS (Bardeen et al. 1986) transfer function, which does not take into account the effect of baryons at all, instead of the Ma (1996) transfer function, which does take it into account for  $\Omega_b h^2 = 0.0125$  with  $h = 0.5$ , gives essentially the same column density distribution for the range of column densities discussed here. For models where the baryon content is proportionally higher, Low-density Cold Dark Matter Models for instance, changing  $\Omega_b h^2$  has a more pronounced effect on the transfer function.

## 6.2. Dependence on the Equation of State or the Temperature-density Relation

Let us hold fixed  $T_0$ ,  $\Omega_b h^2$  and  $J_{\text{HI}}$  at their canonical values as shown in equation (32) but allow the equation of state to change, for the same CDM model as above. As is pointed out in Sec. 3.2, the temperature-density relation for low enough overdensity is well-approximated by a power law where the power index is around 0.5, but can change slightly depending on the reionization history. We plot in Fig. 8 the column density distributions for  $\gamma = 1.2, 1.5, 1.7$  where  $\gamma$  is defined by  $T \propto (1 + \delta_b)^{\gamma-1}$ . It should adequately cover the possible range of  $\gamma$  (Hui & Gnedin 1996).

The first thing to notice is that the column density distribution remains almost the same for the three different values of  $\gamma$ . This is because  $\gamma$  affects column density through the power index of  $(1 + \delta_b)$ , which is  $2 - 0.7(\gamma - 1)$  (eq. [28]). The index does not change significantly for the range of  $\gamma$  considered. A larger index (smaller  $\gamma$ ) means for a density peak with a given  $1 + \delta_b$  (and its second derivative), the column density is larger or smaller depending on whether  $1 + \delta_b$  is bigger or smaller than one. The net effect is to decrease the slope of the column density distribution. The effect, though very small for the values of  $\gamma$  plotted, can still be seen in Fig. 8. We also show the approximate slopes given by an analytical formula (eq. 39) which will be discussed later. Note how the column density distribution does not exactly follow a power law but can be approximated by one.

Hence as a crude approximation, we conclude that the mean temperature, radiation intensity and baryon density mainly determine the overall normalization of the column density distribution. The equation of state, on the other hand, mostly affects the slope of the column density distribution but its effect is small for reasonable range of  $\gamma$ .

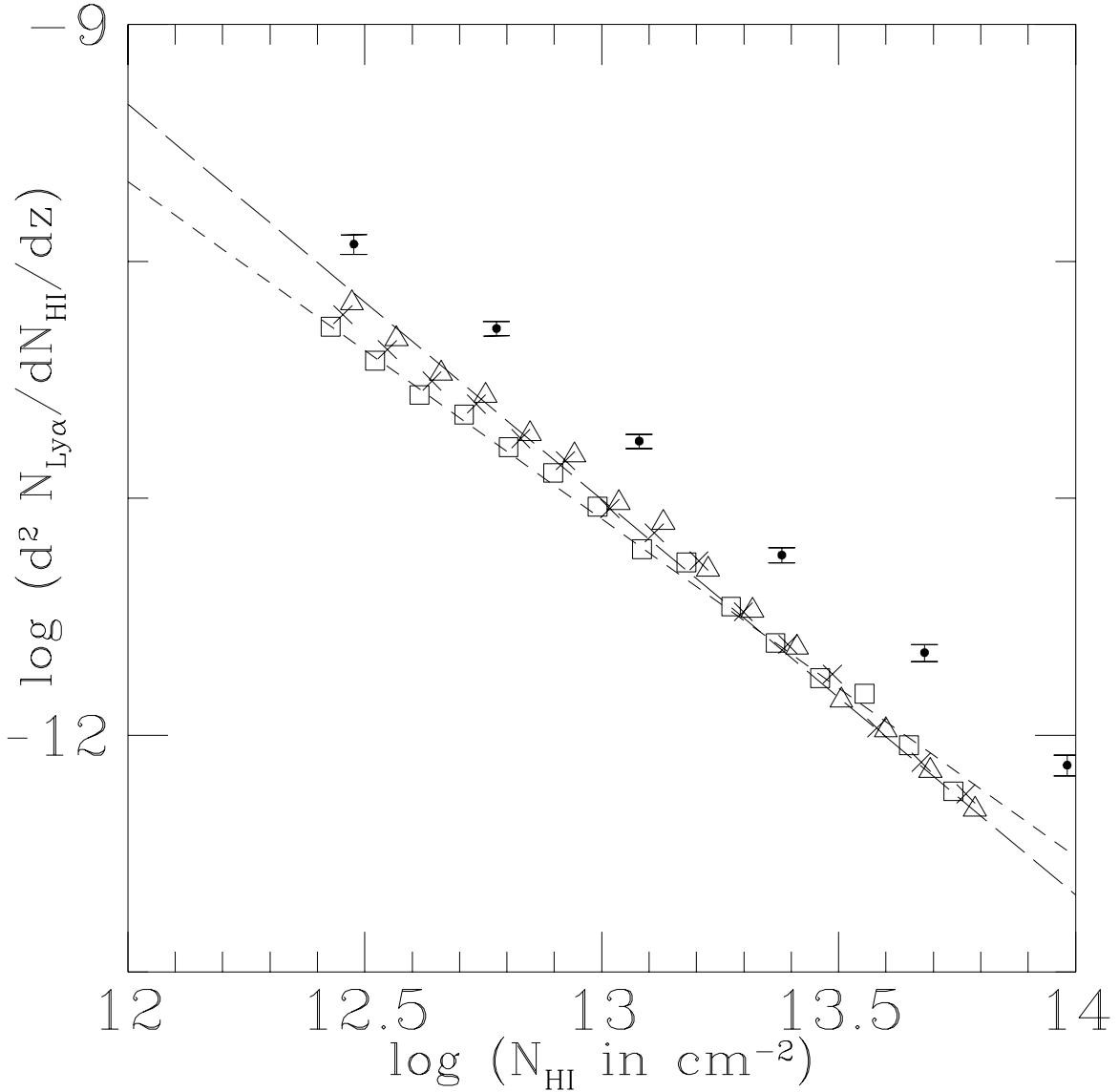


Fig. 8.— Column density distributions of the CDM1 model (Table 1) for three different equations of state (eq. [19]). Open squares:  $\gamma = 1.2$ ; crosses (same as crosses in Fig. 7):  $\gamma = 1.5$ ; open triangles:  $\gamma = 1.7$ .  $F = 1$  (defined in eq. [32]) for all three. Points with error-bars are the same observational data as in Fig. 7. Long-dashed and short-dashed lines have the approximate slopes ( $\beta = 1.67$  and  $\beta = 1.43$ ) (normalization is chosen by hand) as given in equation (39) for the open triangles and open squares respectively.

### Dependence on $\sigma_8$

Putting  $\gamma = 1.5$  and  $F = 1$  (eq. [32]), we now consider CDM models with different  $\sigma_8$ , in other words, different normalizations of the power spectrum. Plotted in Fig. 9 are two CDM models, one with  $\sigma_8 = 0.7$ , the other with  $\sigma_8 = 0.4$ , both without any tilt. Both have the same thermal and ionization parameters ( $T_0 = 10^4$  K,  $J_{\text{HI}} = 0.5$  and  $\gamma = 1.5$ ). The  $\sigma_8 = 0.4$  model is not meant to be realistic but it serves to illustrate the effect of choosing a different normalization.

It is interesting to see that changing the normalization of the power spectrum alters the slope of the column density distribution. For column densities greater than about  $10^{12.5}$  cm $^{-2}$ , the lower  $\sigma_8$  model has a steeper distribution. It indicates that the model is in a more “linear” state of evolution compared with the higher  $\sigma_8$  model at a redshift of 3. There are proportionally more low density peaks compared to high density ones, hence the steeper distribution. For sufficiently low column densities, however, the absorption lines arise from very underdense regions which should be more common in the high  $\sigma_8$  model. Hence at very low column densities, the high  $\sigma_8$  model should win: it has more very low density peaks. Where this might occur we cannot tell from our simulations because of the limited resolution. For the range of column densities we can measure reliably, the slope of the column density distribution simply steepens as  $\sigma_8$  is lowered.

### Dependence on the Shape of the Power Spectrum

We investigate here the effect of changing the slope of the power spectrum while keeping  $\sigma_8$  fixed. Fig. 10 shows two CDM models, both with  $\sigma_8 = 0.7$ , one without tilt and the other with the spectral index  $n = 0.7$ . Small scale power is suppressed in the  $n = 0.7$  model. The effect on the column density distribution is very similar to lowering  $\sigma_8$ .

Another way to alter the shape of the power spectrum is to apply different amounts of smoothing to the *same* initial power spectrum.

In Fig. 11, we plot for the  $\sigma_8 = 0.7$  CDM1 model (Table. 1) the results of three different smoothing scales. The crosses represent the result of using the smoothing scale according to the standard prescription (eq. [15]). More smoothing (open triangles) has qualitatively the same effect as lowering  $\sigma_8$  (Fig. 9). This should come as no surprise because smoothing means decreasing small scale power. Again, one ends up decreasing the number of high density peaks compared to low density peaks, hence resulting in a steeper column density distribution. Smoothing by  $k_S = 1.15$  Mpc $^{-1}$  removes more structure than is necessary from the point of view of optimizing the truncated Zel’dovich approximation. Smoothing by  $k_S = 8.4$  Mpc $^{-1}$  (open squares) has the opposite effect of making the column density distribution flatter, but it should be kept in mind that severe orbit-crossing occurs because

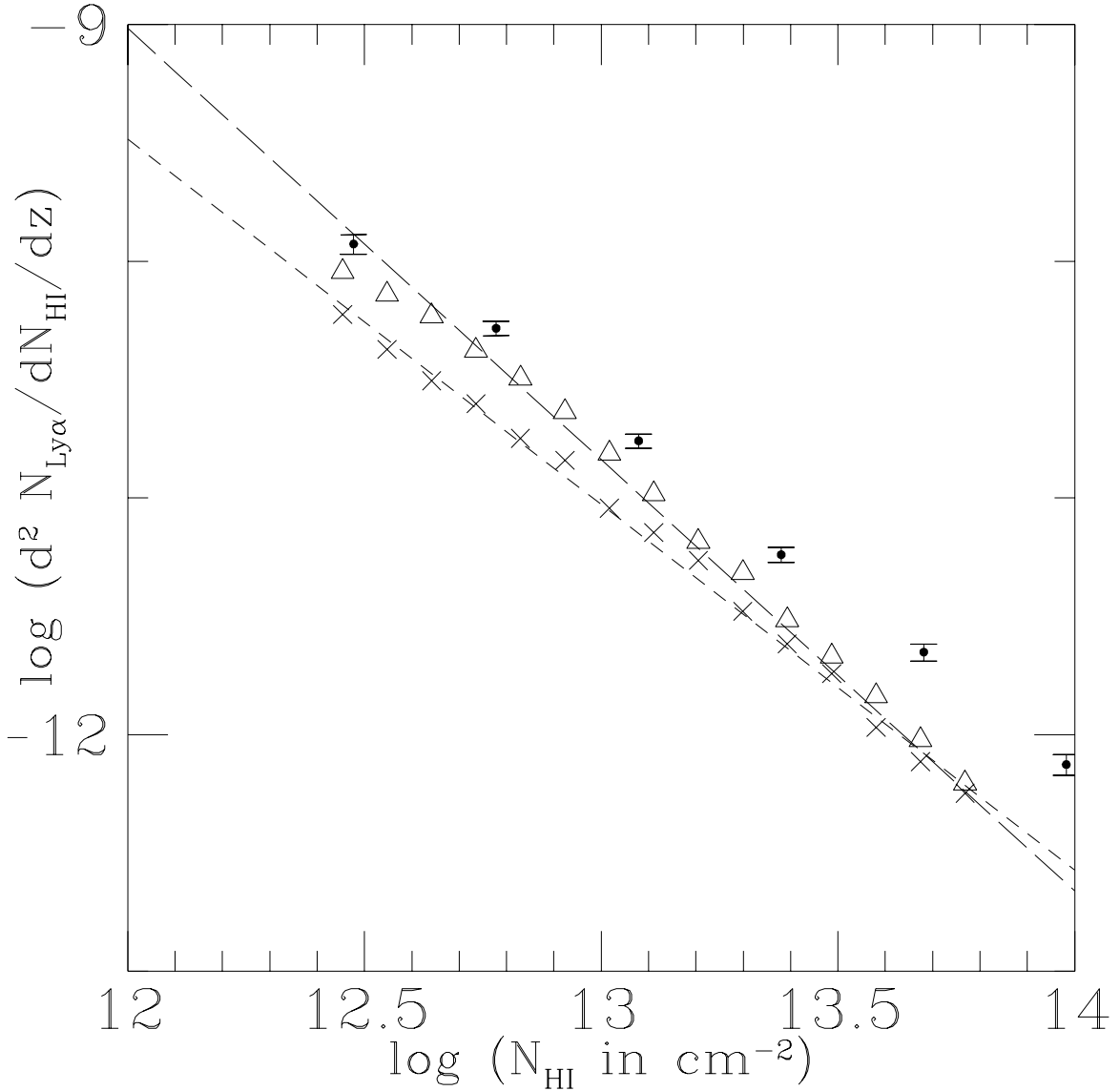


Fig. 9.— Points with error-bars are the same observational data as in Fig. 7. Crosses (same as crosses in Fig. 7): the CDM1 model with  $\sigma_8 = 0.7$  (see Table 1). Open triangles: the CDM3 model with  $\sigma_8 = 0.4$ . For both models,  $F = 1$  (eq. [32]) and  $\gamma = 1.5$  (eq. [19]) are adopted. The long-dashed and short-dashed lines have the approximate slopes ( $\beta = 1.82$  and  $\beta = 1.54$ ) as given in equation (39) for the open triangles and crosses respectively.

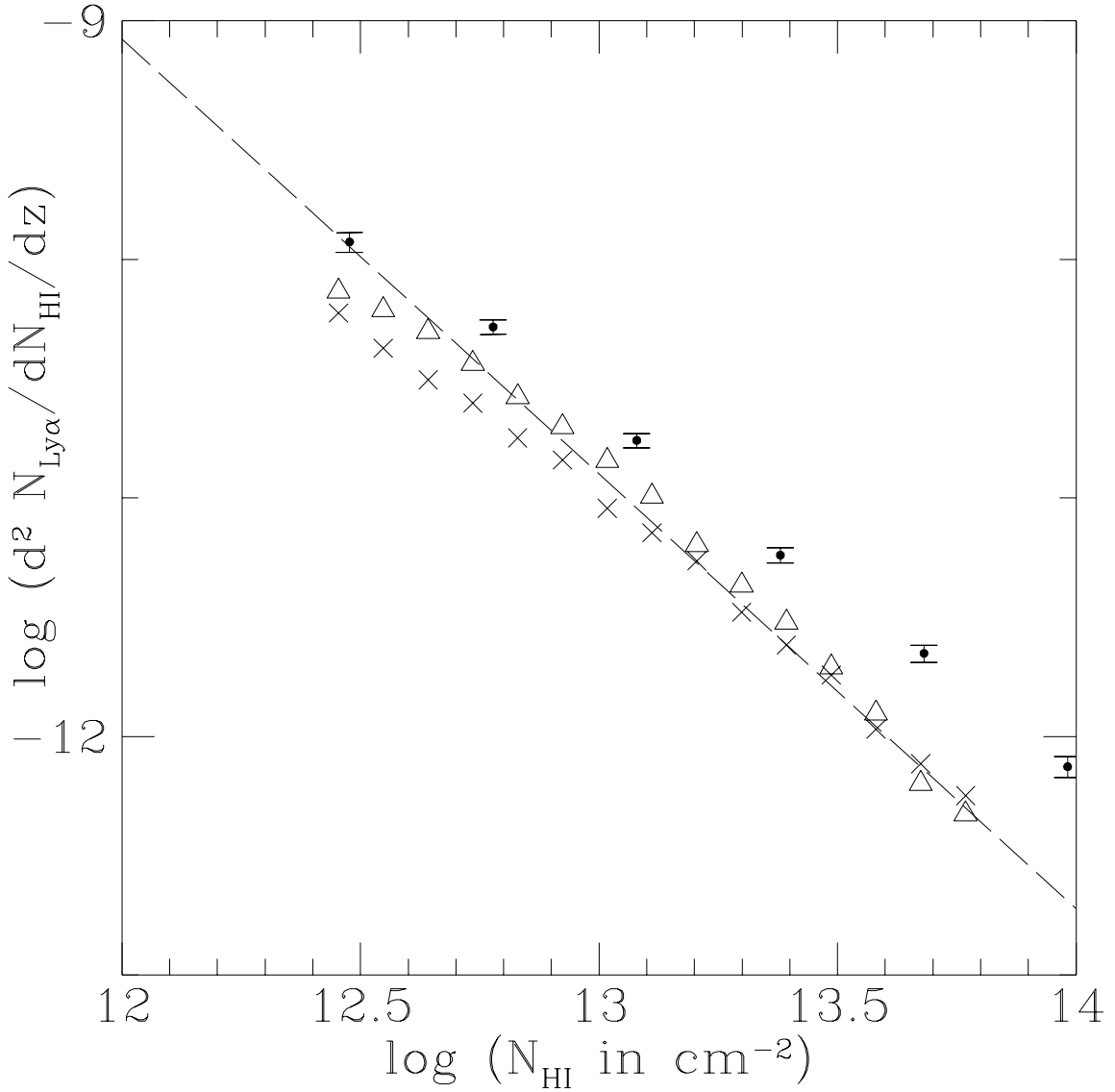


Fig. 10.— Points with error-bars are the same observational data as in Fig. 7. Crosses represent the  $\sigma_8 = 0.7$  and no tilt CDM1 model as before (same as crosses in Fig. 7; see Table 1). Open triangles represent the column density distribution of the CDM4 model:  $\sigma_8 = 0.7$  with tilt, the spectral index being 0.7. For both models,  $F = 1$  (eq. [32]) and  $\gamma = 1.5$  (eq. [19]) are adopted. The dashed line has the approximate slope ( $\beta = 1.82$ ) as given in equation (39) for the open triangles.

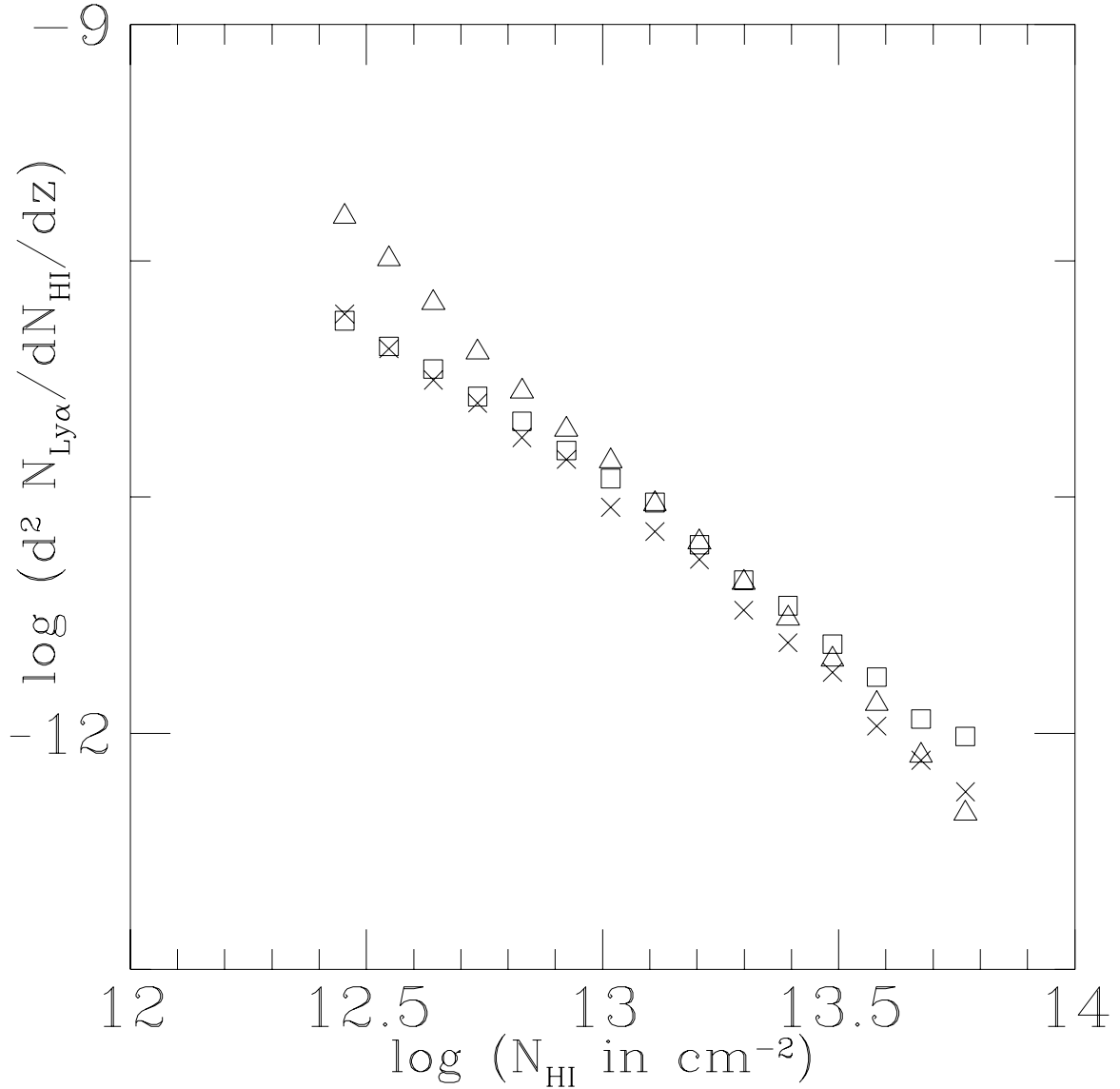


Fig. 11.— Column density distributions of the CDM1 model (Table 1) for three different initial smoothing scales. Crosses (same as crosses in Fig. 7):  $k_S = 2.3 \text{ Mpc}^{-1}$ , which is the smoothing scale according to the standard prescription (eq. [15]). Open triangles:  $k_S = 1.15 \text{ Mpc}^{-1}$ . Open squares:  $k_S = 8.4 \text{ Mpc}^{-1}$ , which is the Jeans scale for  $T_0 = 1$  and  $\gamma = 1.5$ . We adopt  $F = 1$  (eq. [32]) and  $\gamma = 1.5$  (eq. [19]) for all three cases.

not enough smoothing is performed in this case. The comparison with a full hydrodynamic simulation in Fig. 5 lends support to the standard prescription for choosing  $k_S$  (eq. [15]).

To understand the overall effect of altering the power spectrum, we plot in Fig. 12 the smoothing scale  $k_S$  versus the following quantity:

$$\sigma_0 = D_+(t) \sqrt{\int_0^\infty 4\pi k^2 P(k) e^{-(k/k_S)^2} dk}. \quad (34)$$

which is the linear rms fluctuation of a density field smoothed with a spherically symmetric Gaussian window with radius  $1/k_S$ . (Note that the Zel'dovich approximation with initial smoothing corresponds to replacing eq. [14] by the above.) The linear growth factor  $D_+(t)$  is equal to  $(1 + \bar{z})^{-1}$  if  $D_+ = 1$  today is assumed. It is one way to represent the amount of fluctuation around comoving scale  $1/k_S$ . Three power spectra are shown: CDM1, CDM3 and CDM4 (see Table 1), all at  $\bar{z} = 3$ . The Jeans scale is around  $8 \text{ Mpc}^{-1}$  for  $T_0 = 10^4 \text{ K}$  (Appendix A), below which we expect the intergalactic medium to be smooth (except for very small scales which have collapsed to form stars, etc) and so does not contribute significantly to absorption lines. For scales large enough such that  $\sigma_0$  is smaller than, say 0.1, the density fluctuations are essentially linear. These are scales that would collapse later to form the larger scale structure we see today. The intergalactic medium is also smooth on those scales at  $\bar{z} = 3$ . This leaves around one to two decades of length scales below  $8 \text{ Mpc}^{-1}$ , on which the density fluctuations contribute to the absorption lines of column densities of interest in this paper. Models with similar  $\sigma_0$  on these scales are therefore expected to have similar column density distributions. (We reached similar conclusions in a separate paper using the lognormal approximation). From Fig. 12, one can then understand why the  $\sigma_8 = 0.4$  model and the  $n = 0.7$ ,  $\sigma_8 = 0.7$  have qualitatively similar column density distribution. Namely, both have smaller  $\sigma_0$  on the relevant scales compared with the  $\sigma_8 = 0.7$  no-tilt-model and hence both have steeper column density distribution for column densities higher than about  $10^{12.5} \text{ cm}^{-2}$ .

## 7. The Slope of the Column Density Distribution

It has been shown that while the normalization of the column density distribution is influenced by the thermal and ionization states of the intergalactic medium which are not well-constrained observationally, the slope is sensitive to the amount of small scale power and the equation of state or the temperature-density relation. We develop an expression for the slope of the column density distribution distribution here.

From equations (27) and (28), it can be seen that the column density  $N_{\text{HI}}$  is proportional to  $(1 + \delta_b)^{2-0.7(\gamma-1)}$  times  $1/\sqrt{\xi''}$ , which basically defines a length scale. Taking into account

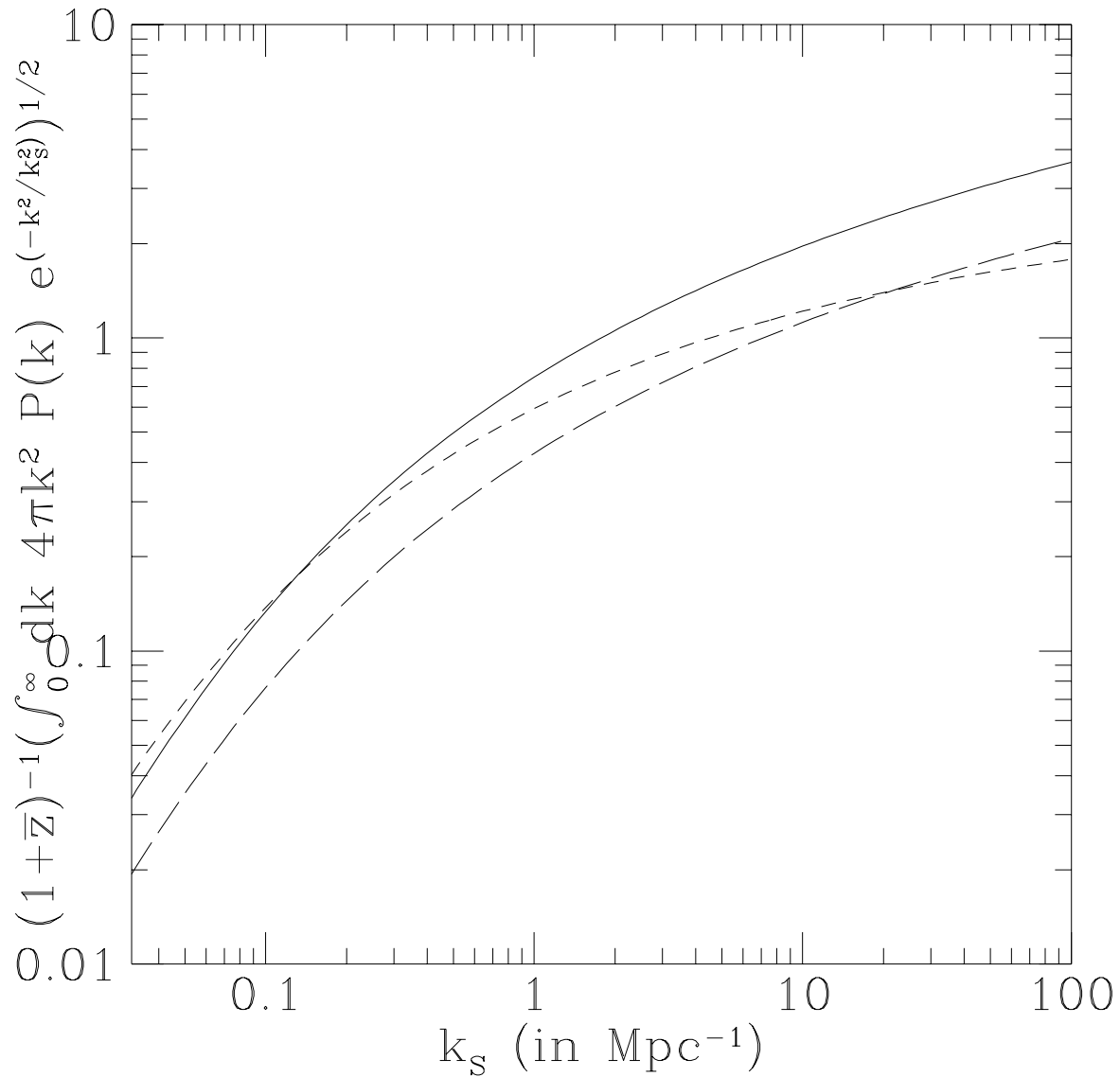


Fig. 12.—  $\sigma_0$  versus  $k_S$  (eq. [34]) at  $\bar{z} = 3$ . Solid line:  $\sigma_8 = 0.7$  CDM with no tilt (CDM1); short dash:  $\sigma_8 = 0.7$  CDM with tilt, spectral index being 0.7 (CDM3); long dash:  $\sigma_8 = 0.4$  CDM with no tilt (CDM4).

the correlation between this length scale and the overdensity, we find from our simulations (which use the Zel'dovich approximation) a useful approximate relation for column densities between about  $10^{12.5}$  and  $10^{14.5} \text{ cm}^{-2}$ :

$$N_{\text{HI}} \propto (1 + \delta_b)^{1.1 - 0.7(\gamma - 1)}, \quad (35)$$

which roughly means the length scale  $1/\sqrt{\xi''}$  is approximately proportional<sup>11</sup> to  $(1 + \delta_b)^{-0.9}$ .

Now, since we are interested in the slope of the column density distribution, the relevant quantity to consider is:

$$-\beta \equiv \frac{d \ln \frac{d^2 N_{\text{Ly}\alpha}}{d N_{\text{HI}} dz}}{d \ln N_{\text{HI}}} = -1 + \frac{m}{1.1 - 0.7(\gamma - 1)}, \quad m \equiv \frac{d \ln \int_{-\infty}^0 d\xi'' |\xi''| P(\xi, \xi' = 0, \xi'')}{d\xi}. \quad (36)$$

The equality follows from equations (35), (27), (29) and (31) and noting that  $\xi \equiv 1 + \delta_b$ . The column density distribution can be approximated by the simple power law  $N_{\text{HI}}^{-\beta}$  if  $\beta$  defined above is only weakly dependent on  $\xi$  or  $N_{\text{HI}}$ .

Now, lacking an analytical expression for  $P$  under the Zel'dovich approximation, we can nonetheless guess what the general properties of the quantity  $m$  are. First of all,  $m$  depends on  $\xi$  in general because the integral  $\int_{-\infty}^0 d\xi'' |\xi''| P(\xi, \xi' = 0, \xi'')$  cannot be a simple power law in  $\xi$ . This is because we expect the integral to vanish for very large and very small  $\xi$  and peak at some intermediate  $\xi$ . This implies one should not expect an exact power-law for the column density distribution, although pieces of it might be approximated by power-law. Suppose  $\xi_{\text{pk}}$  is the value of  $\xi$  where the integral  $\int_{-\infty}^0 d\xi'' |\xi''| P(\xi, \xi' = 0, \xi'')$  reaches its maximum value, then the column densities we are interested in must correspond to  $\xi > \xi_{\text{pk}}$  where  $d \ln \int_{-\infty}^0 d\xi'' |\xi''| P(\xi, \xi' = 0, \xi'')/d\xi$  is negative. This is based on the knowledge that the computed (as well as observed) slope in equation (36) is less than  $-1$  (the factor  $1.1 - 0.7[\gamma - 1]$  is always positive i.e.  $\gamma > 1$ ). Furthermore, as we have noted before, we expect the relative number of high density to intermediate density (for  $\xi$  larger than  $\xi_{\text{pk}}$ ) peaks to be lower for models with less power, which means  $m$  is more negative. Lastly, since the Zel'dovich displacement field is Gaussian in Lagrangian space, we expect on quite general grounds that  $P(\xi, \xi', \xi'')$  depends on the power spectrum through the 3 parameters:  $\sigma_0$  as defined in equation (34) and  $\sigma_1$  and  $\sigma_2$  defined as follows (see Bardeen et al. 1986):

$$\sigma_1 = D_+(t) \sqrt{\int_0^\infty 4\pi k^4 P(k) e^{-(k/k_s)^2} dk}, \quad \text{and} \quad \sigma_2 = D_+(t) \sqrt{\int_0^\infty 4\pi k^6 P(k) e^{-(k/k_s)^2} dk}, \quad (37)$$

---

<sup>11</sup>A log-log plot of  $1/\sqrt{\xi''}$  versus  $(1 + \delta_b)$  actually shows a lot of scatter but equation (35) appears to capture the overall dependence of  $N_{\text{HI}}$  on  $1 + \delta_b$ .

where  $D_+$  is the linear growth factor which is equal to  $(1 + \bar{z})^{-1}$  for a universe at critical matter density, where  $k_S$  is the smoothing scale defined in equation (15) or (16), according to the prescription described in Sec. 3.1.

Bardeen et al. (1986) defined the following parameters:

$$R_* \equiv \sqrt{3} \frac{\sigma_1}{\sigma_2}, \quad \gamma_B \equiv \frac{\sigma_1^2}{\sigma_2 \sigma_0}, \quad (38)$$

where we have renamed  $\gamma_B$  to distinguish it from  $\gamma$  we use in this paper. Hence,  $P(\xi, \xi', \xi'')$  can be viewed as depending on  $\sigma_0$ ,  $R_*$  and  $\gamma_B$ . It can be shown that this quantity does not depend on  $R_*$  if  $\xi'$  is restricted to zero except for a multiplicative factor (see Gnedin and Hui 1996 for example) whereas  $\gamma_B$  is around 0.5 for all the models we consider in this paper. Hence, as a crude approximation, one can regard  $m$  defined in equation (36) as depending on  $\sigma_0$  only.<sup>12</sup> Bearing in mind,  $\sigma_0$  is always close to 1, one can imagine taking a Taylor series expansion of  $m$  around 1 and keeping only the first order term. We find that the following expression for  $\beta$  fits reasonably well the slope of the column density distributions for the CDM and CHDM models we study:

$$\beta = 1 + \frac{1}{1.1 - 0.7(\gamma - 1)} [0.54 - 1.1(\sigma_0 - 1)], \quad (39)$$

where  $\beta$  satisfies equation (36). Examples of how well it describes the variation of the slope with the power spectrum and the equation of state can be found in Figures 8, 9, 10, 16, 17, 18 and 19.

The above form for  $\beta$  displays the expected dependence of the slope on  $\sigma_0$ , namely steeper slope with lower  $\sigma_0$ . We can also see that it is possible to find combinations of *gamma* around 1.4 and  $\sigma_0$  around 1.1 that reproduce the observed value  $\beta \sim 1.5$ . We emphasize, however, that the actual column density distribution is only approximately described by a power-law as can be seen in one of the figures mentioned above.

## 8. The Column Density Distribution for CHDM models

In Sec. 6, we learn that while  $T_0$ ,  $J_{\text{HI}}$  and  $\Omega_b h^2$  play a major role in determining the normalization of the column density distribution, the amount of power on comoving scales between around  $1 \text{ Mpc}^{-1}$  and  $10 \text{ Mpc}^{-1}$  is primarily responsible for its shape or slope. The equation of state also has a small effect on the slope of the column density distribution.

---

<sup>12</sup>Now,  $m$  should depend on  $\xi$  in general too, but the range of  $\delta_b$  ( $\xi \equiv \ln[1 + \delta_b]$ ) that is responsible for the column densities we are interested in is also of the order of  $\sigma_0$ .

Label	$\sigma_8$	$n$	$k_S/\text{Mpc}^{-1}$	$\Omega_b$	$\sigma_0$
CDM1	0.7	1.0	2.3	0.05	1.12
CDM2	0.7	1.0	2.3	0.06	1.12
CDM3	0.4	1.0	5.86	0.05	0.93
CDM4	0.7	0.7	3.58	0.05	0.93

Table 1: A list of all the CDM models discussed in this paper. All have  $h = 0.5$ . The spectral index of the power spectrum is  $n$ . Every model has  $\Omega_b = 0.05$  except for CDM2, which has a higher baryon content and is shown in Fig. 5. The truncation scale  $k_S$  is defined by  $k_S = 1.5 k_{\text{NL}}$  (eq. [15]). The rms density fluctuation  $\sigma_0$  is defined in equation (34), for the value of  $k_S$  given here. We assume  $\bar{z} = 3$ . The rms linear density fluctuation in a sphere of radius  $8h^{-1} \text{ Mpc}$  is equal to  $\sigma_8$ .

Label	$\Omega_\nu$	$h$	$n$	$Q_{\text{rms}}/\mu\text{K}$	$T/S$	$k_S/\text{Mpc}^{-1}$	$\sigma_0$
A1	0.1	0.5	0.95	18.5	$7(1-n)$	3.8	1.08
A2	0.2	0.5	0.95	18.5	$7(1-n)$	8.4	0.84
A3	0.3	0.5	0.95	18.5	$7(1-n)$	not apply	not apply
B1	0.1	0.5	0.9	19.2	0	3.3	1.08
B2	0.2	0.5	0.9	19.2	0	8.4	0.87
C1	0.1	0.65	0.9	19.2	$7(1-n)$	3.1	1.09
C2	0.2	0.65	0.9	19.2	$7(1-n)$	10.9	1.02
D1	0.1	0.65	0.8	20.5	0	2.8	1.08
D2	0.2	0.65	0.8	20.5	0	10.9	1.02

Table 2: A list of all the CHDM models discussed in this paper. All have  $\Omega_b = 0.05$ . The parameters are defined as follows:  $\Omega_\nu$  is the density parameter in neutrino,  $n$  is the spectral index of the power spectrum,  $Q_{\text{rms}}$  is the COBE quadrupole in  $\mu\text{K}$  and  $T/S$  is the tensor to scalar ratio. The smoothing wavenumber  $k_S$  for each  $\Omega_\nu = 0.1$  model is  $1.5 k_{\text{NL}}$  (eq. [15]) and  $k_S$  for each  $\Omega_\nu = 0.2$  model is the Jeans scale for  $\gamma = 1.5$ ,  $T_0 = 10^4 \text{ K}$  and the corresponding  $h$  (see Sec. 3.2). No simulation is run for A3, so no  $k_S$  is listed. The rms linear density fluctuation  $\sigma_0$  is defined in equation (34), for each value of  $k_S$  given in the seventh column. The models and their power spectra are taken from Ma (1996).

We apply these insights to study a group of CHDM models. They are all  $\Omega_0 = 1$  models with  $\Omega_b = 0.05$ . Both the  $\Omega_\nu = 0.2$  and  $\Omega_\nu = 0.1$  versions are considered. They have been shown to give good agreement with the observational data on large scales ( $k$  around  $0.02 - 0.4 \text{ Mpc}^{-1}$ ) (see Fig. 6 and 7 of Ma 1996). The  $\Omega_\nu = 0.3$  models seem to conflict with observed abundance of damped Ly $\alpha$  systems, which correspond to roughly  $k$  around  $0.1 - 1.0 \text{ Mpc}^{-1}$  comoving in the linear power spectrum. (Mo & Miralda-Escudé 1994; Kauffmann & Charlot 1994; Ma & Bertschinger 1994). We list in Table 2 the CHDM models considered in this paper. We include one  $\Omega_\nu = 0.3$  CHDM model for the sake of comparison. As is shown convincingly by Ma (1996), all models need some amount of tilt to match observations.

We compute as before the column density distribution for each model using the Density-Peak-Ansatz and the Zel'dovich approximation with appropriate smoothing. The (density weighted) power spectrum for each CHDM model is taken from Ma (1996).

As we have discussed before in the context of the CDM models, a plot of rms smoothed linear density fluctuation  $\sigma_0$  versus smoothing scale  $k_S$  (eq. [34]) is a very good indicator of what column density distribution to expect. This is done in Fig. 13 for the CHDM models tabulated in Table 2. The no-tilt  $\sigma_8 = 0.7$  CDM model is also plotted for comparison.

Because of neutrino free streaming, all CHDM models have less power than the CDM model on small scales. Those with more neutrino content ( $\Omega_\nu = 0.2$ ) have even less power than the others. In fact, the  $\Omega_\nu = 0.2$  models have  $\sigma_0 < 1$  on all scales larger than the Jeans scale ( $k_S < k_J$ ). One expects the Zel'dovich approximation to work particularly well for these models because the amount of orbit-crossing will not be significant, even without initial truncation.

This is borne out by the next test: we compute the column density distribution for one CHDM model B2 and examine the effect of choosing different smoothing scales. The result is plotted in Fig. 14. The column density distribution in the range plotted does not change much at all for the three different smoothing scales plotted. Contrast this with the case of  $\sigma_8 = 0.7$  CDM (Fig. 11) where the column density distribution is more sensitive to changes in the smoothing scale. That's why the truncation scale has to be chosen with some care for the CDM models: not too small ( $k_S$  too big) so that too much orbit crossing has occurred and not too large so that too much small scale structure is erased. We have shown the standard prescription (Sec. 3.1) to be a good one in Sec. 5.

For the CHDM model considered (in fact, it holds true for all other  $\Omega_\nu = 0.2$  models here), the amount of small scale power is so insignificant that excluding them by smoothing does not affect the overall column density distribution at all (except possibly that one loses

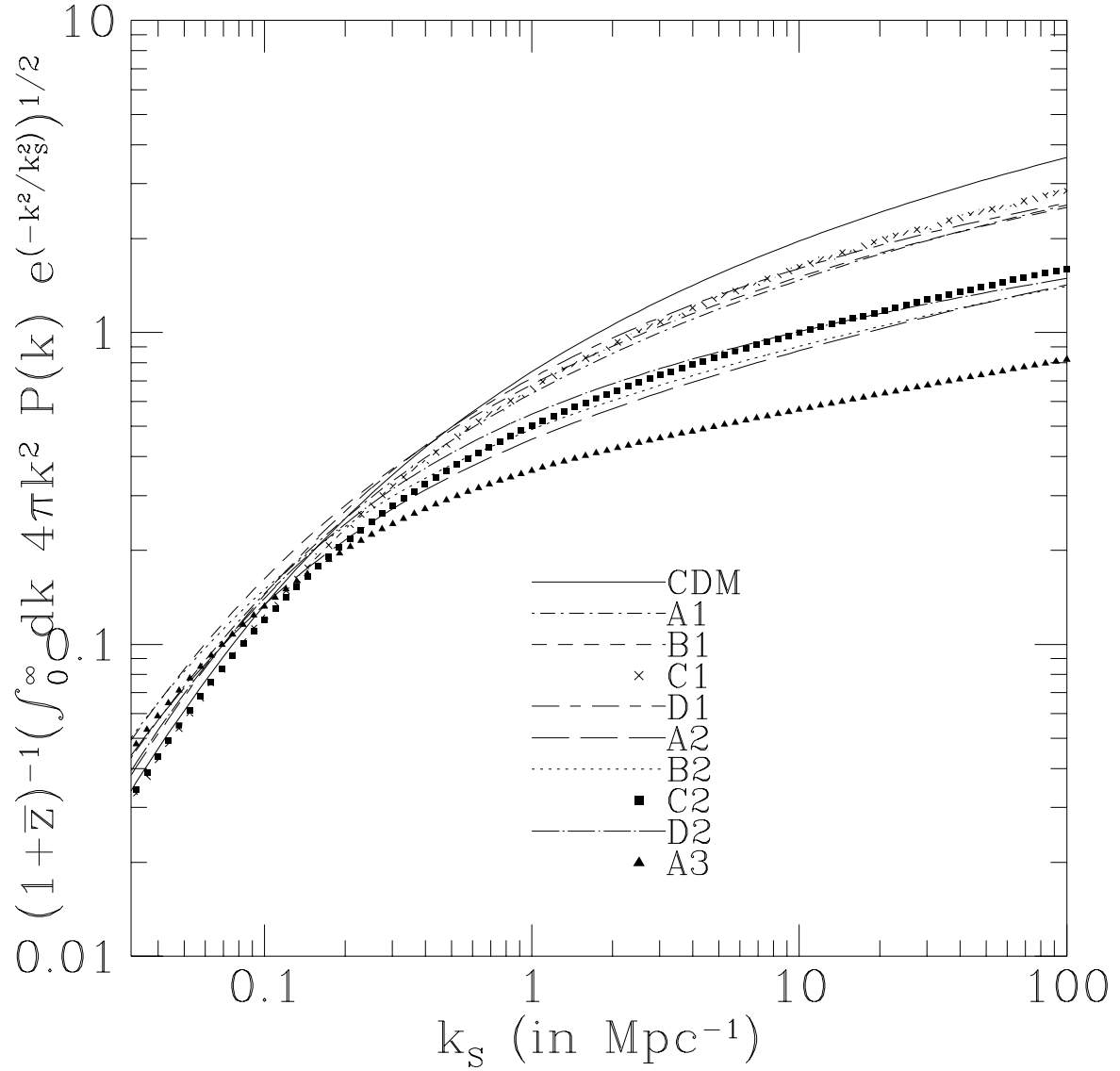


Fig. 13.— Going from the top, the solid line is the same  $\sigma_8 = 0.7$ ,  $h = 0.5$  CDM model with no tilt as in Fig. 7; the next four sets of points/lines close together are all  $\Omega_\nu = 0.1$  CHDM models, A1, B1, C1 and D1 in Table 2 ; the next four sets are all  $\Omega_\nu = 0.2$  CHDM models, A2, B2, C2 and D2; the last set, solid triangles, is an  $\Omega_\nu = 0.3$  CHDM model, A3. All are shown at  $\bar{z} = 3$ .

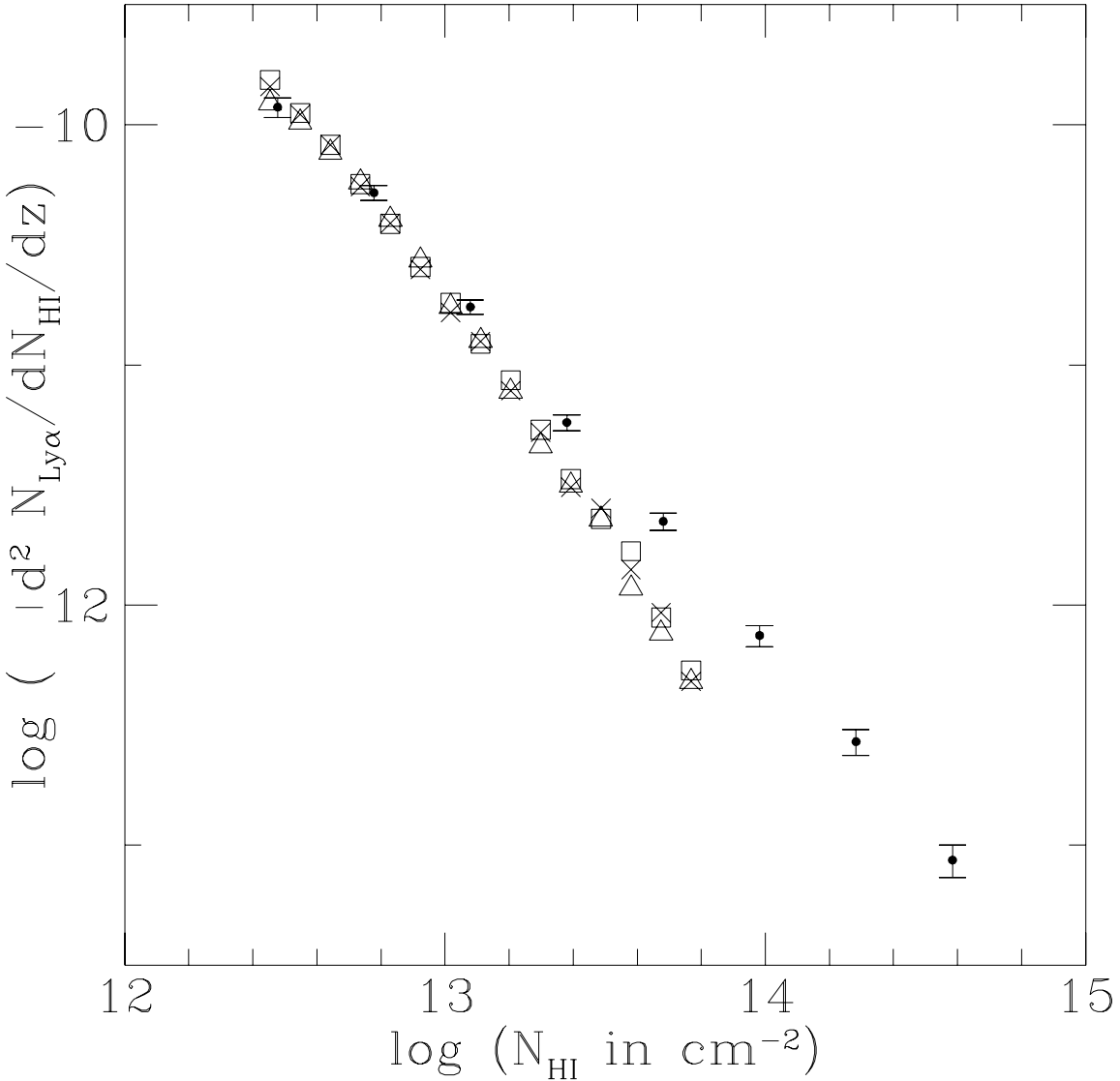


Fig. 14.— Column density distributions of the B2 CHDM model (see Table 2) for three initial smoothing scales. Crosses:  $k_S = 19.2 \text{ Mpc}^{-1}$  (standard truncation prescription,  $k_S = 1.5 k_{\text{NL}}$  according to eq. [15]). Open triangles:  $k_S = 8.4 \text{ Mpc}^{-1}$  (Jeans scale for  $T_0 = 10^4$  and  $\gamma = 1.5$ ). Open squares: no smoothing at all. Points with error-bars are the observational data as in Fig. 7. For all models,  $F = 1$  (eq. [32]) and  $\gamma = 1.5$  (eq. [19]) are used.

the small scale fluctuations that can give rise to very low column density absorption i.e. lower than our resolution limit). We have also done similar tests for the  $\Omega_\nu = 0.1$  models, their response to changes in the truncation scale is somewhere between the  $\sigma_8 = 0.7$  CDM model and the  $\Omega_\nu = 0.2$  CHDM models, as can be expected based on their difference in Fig. 13.

We adopt the following truncation scales for the CHDM models. For the  $\Omega_\nu = 0.1$  models, the standard prescription described in Sec. 3.1 is used (i.e.  $k_S = 1.5 k_{NL}$ ). The  $\Omega_\nu = 0.2$  models, according to the above prescription, would have truncation scales less than the Jeans length ( $k_S > k_J$ ) and so by the arguments presented in Sec. 3.1,  $k_S = k_J$  is adopted. Again, we emphasize that for this class of models that have relatively little power on small scales, the precise truncation scale is not important. A summary of the truncation scales for all models can be found in Table 2.

The CHDM models with  $\Omega_\nu = 0.1$  are plotted in Fig. 15. Values of  $F$  that give reasonable match to the observational data are chosen for each model. Note how the low-Hubble-constant-models ( $h = 0.5$ ) requires a slightly lower  $F$  (eq. [32]) than the higher-Hubble-constant-models. The equation of state is chosen to be the same for all models ( $\gamma = 1.5$ , see equation [19]). The level of agreement with the observational data, for the given choices of parameters, is satisfactory. Notice how the low Hubble-constant ( $h = 0.5$ ) models tend to have steeper column density distributions, because they have less power on the relevant scales (see Fig. 13). Their slopes can be brought into better agreement with that of the observational data if a smaller  $\gamma$  is used.

For the  $\Omega_\nu = 0.2$  models, we cannot find values of  $F$  that gives the same level of agreement with observations for  $\gamma = 1.5$ . Two examples are shown in Fig. 17 and Fig. 16. Both have  $h = 0.5$  and small amounts of tilt. For each, three sets of theoretical predictions are plotted, one for each value of  $F$ , 1, 2.5 or 5. For  $\Omega_b h^2 = 0.0125$ , the conventional Big-bang nucleosynthesis value, and  $T_0 = 10^4 K$ , they correspond to radiation intensity  $J_{HI}$  of 0.5, 0.2 and 0.1 (eq. [32]). As we have shown before, changing  $F$  mainly shifts the sets of points without altering the slope significantly. For the column density between about  $10^{12.5}$  and  $10^{14.5} \text{ cm}^{-2}$ , the slope of the predicted distribution seems to be too steep compared to the observational data. The slope is about  $-2$  with some flattening at the lower column densities.

Another  $\Omega_\nu = 0.2$  CHDM model (*D2* in Table 2), which has a higher Hubble constant ( $h = 0.65$ ), is shown in Fig. 18. (The *C2* CHDM model which also has  $h = 0.65$ , gives very similar column density distribution.) The slope of its column density distribution is not as steep as the previous ones. This is expected because the higher Hubble constant models have slightly more power on relevant scales, as is evident in Fig. 13. In fact, one

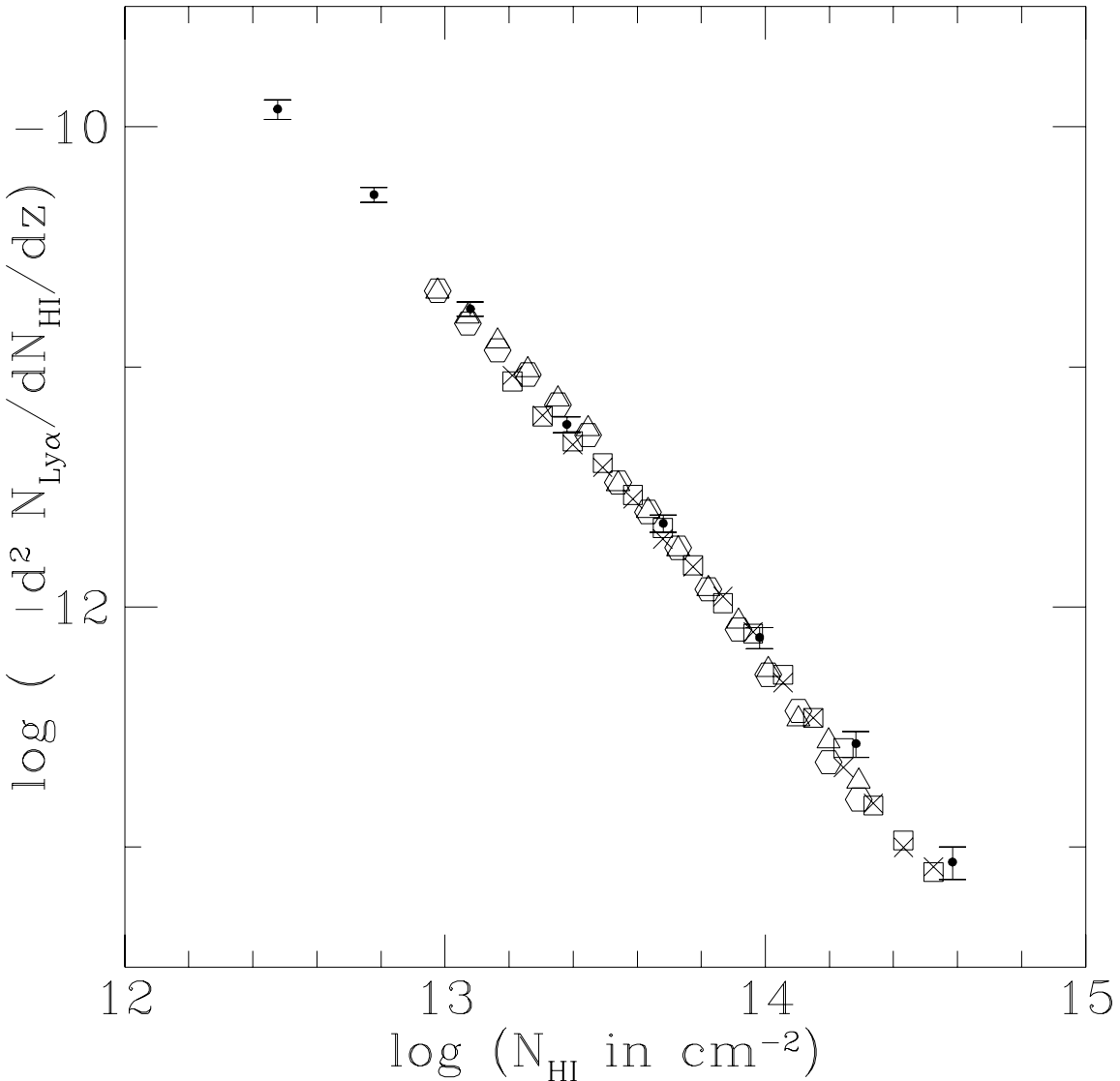


Fig. 15.— Column density distributions for four  $\Omega_\nu = 0.1$  CHDM models. Points with error-bars are the observational data as in Fig. 7. All models have  $\Omega_\nu = 0.1$ . We use  $\gamma = 1.5$  in the equation of state for all of them (eq. [19]). Table 2 contains descriptions of each of the following models. Open hexagons: B1,  $F = 3.33$ . Open triangles: A1,  $F = 3.33$ . Crosses: D1,  $F = 5.7$ . Open squares: C1,  $F = 5.7$ .  $F$  is defined in equation (32).

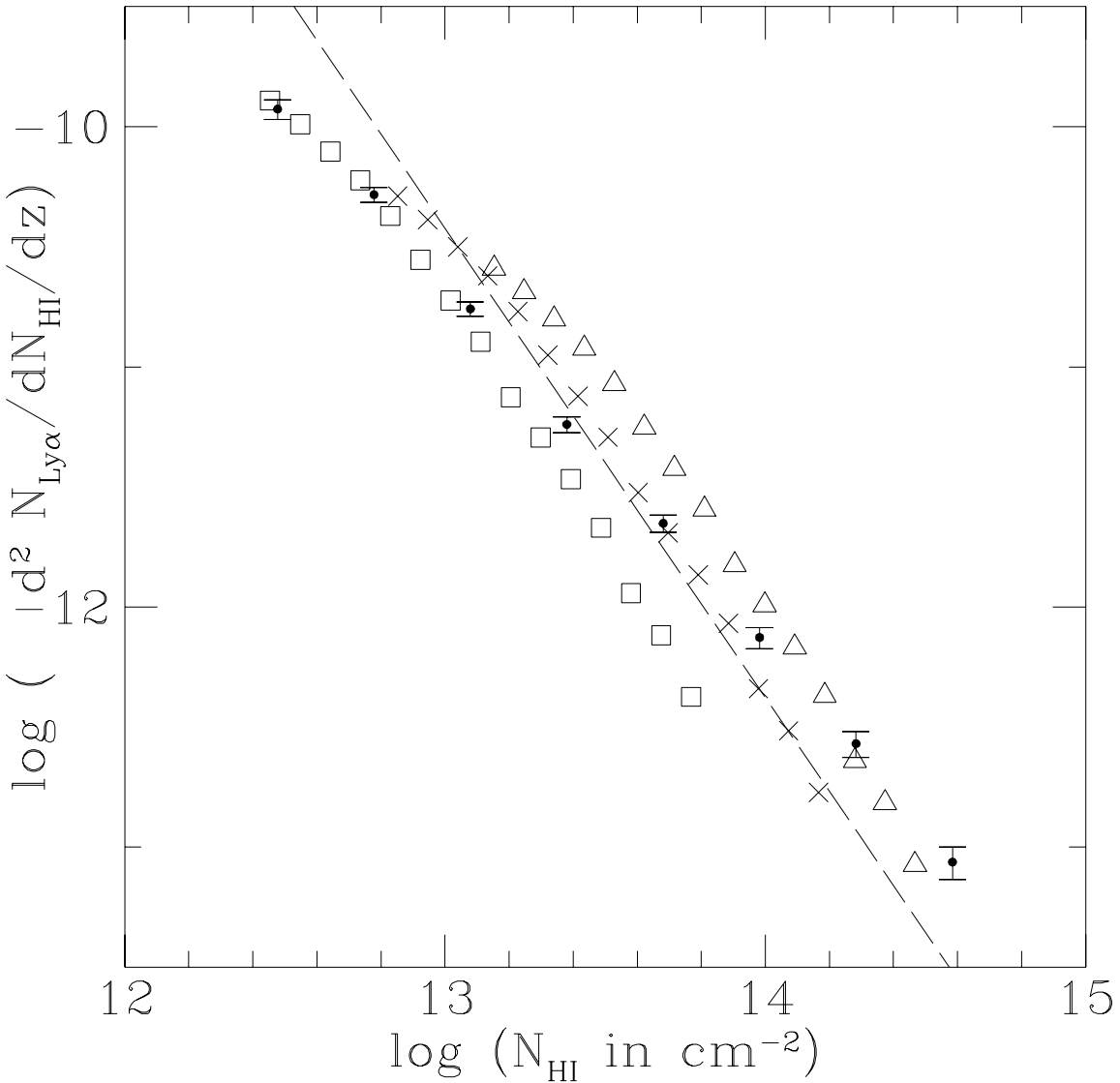


Fig. 16.— The column density distribution for the A2 CHDM model (Table 2). Three values of  $F$  (eq. [32]) are shown:  $F = 1$  (open squares),  $F = 2.5$  (crosses) and  $F = 5$  (open triangles). We choose  $\gamma = 1.5$  for all three (eq. [19]). Points with error-bars are the observational data as in Fig. 7. The dashed line has the slope of  $\beta = 1.95$ , as given in equation (39). The normalization is chosen by hand.

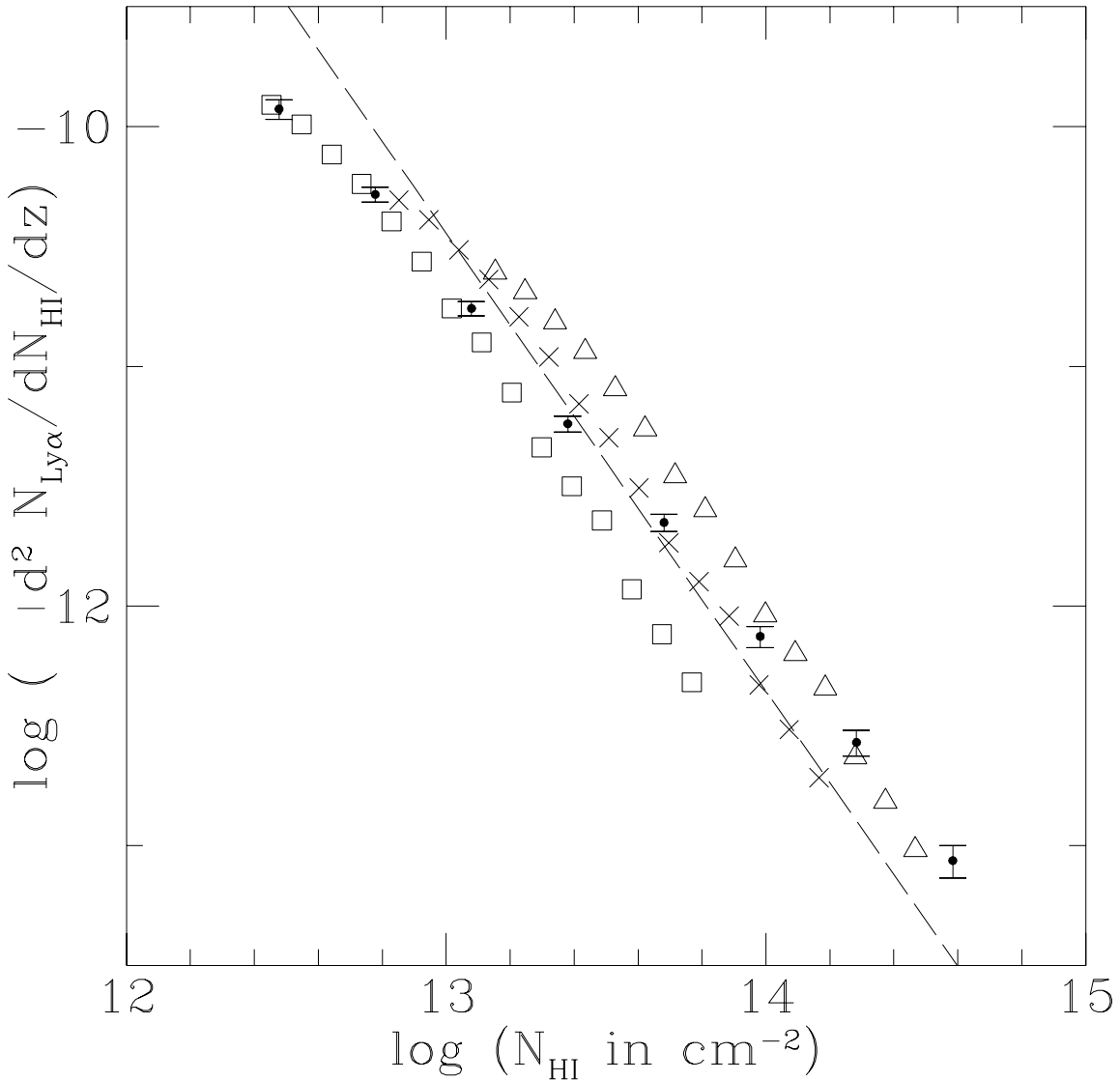


Fig. 17.— The column density distribution for the *B2* CHDM model (Table 2). Three values of  $F$  are shown (eq. [32]):  $F = 1$  (open squares),  $F = 2.5$  (crosses) and  $F = 5$  (open triangles).  $\gamma = 1.5$  for all three (eq. [19]). Points with error-bars are the observational data as in Fig. 7. The dashed line has a slope of  $\beta = 1.91$ , as given in equation (39).

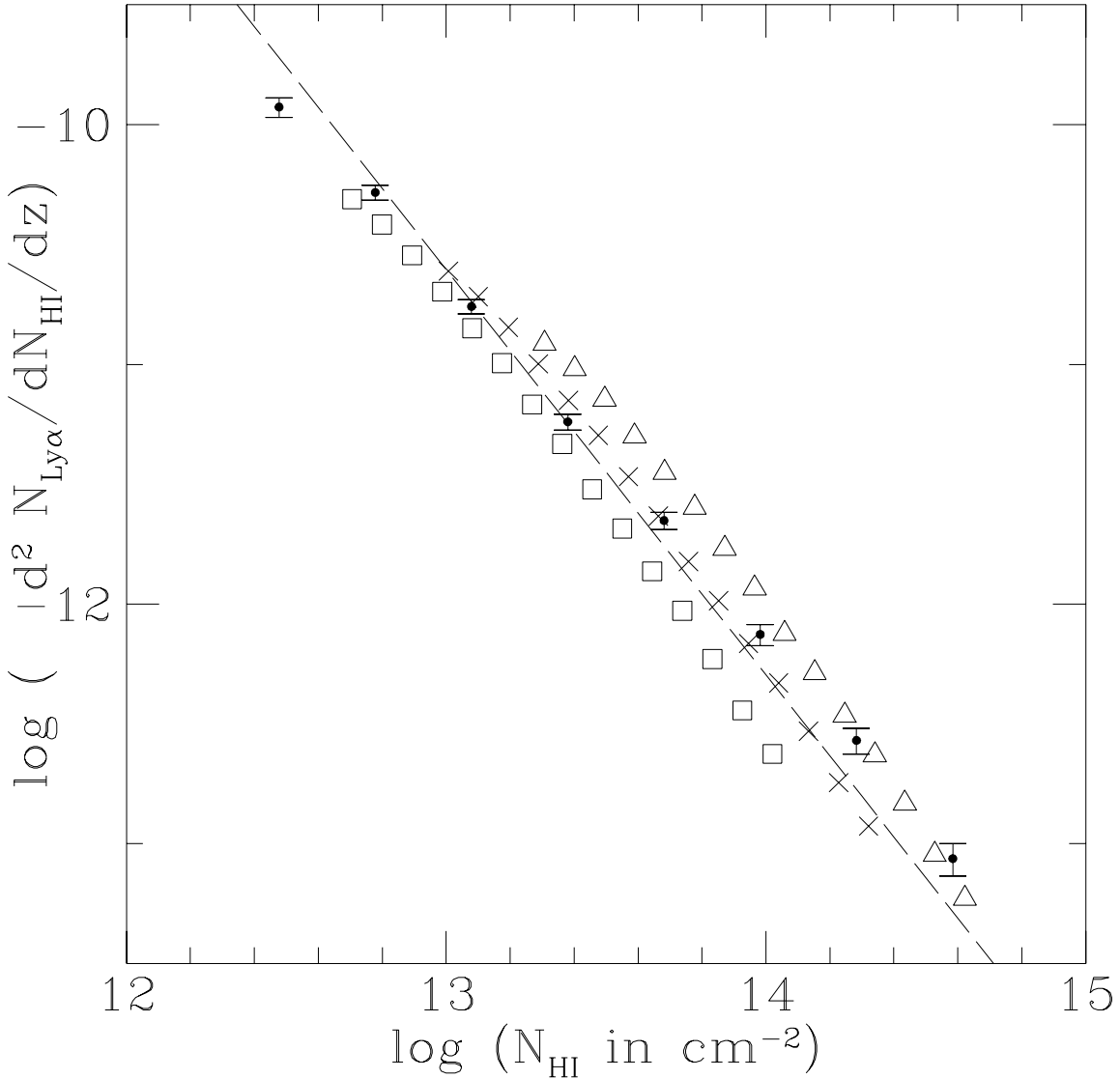


Fig. 18.— The column density distribution for the  $D2$  (Table 2) CHDM model. Three values of  $F$  are shown (eq. [32]):  $F = 7.14$  (open triangles),  $F = 3.57$  (crosses) and  $F = 1.79$  (open squares).  $\gamma = 1.5$  for all three (eq. [19]). Points with error-bars are the same observational data as in Fig. 7. The dashed line has a slope of  $\beta = 1.69$ , as given in equation (39).

might argue that the middle set of points in figure, the one having  $F = 3.57$ , match the observational data reasonably well if both observational and theoretically errors are taken into account. However, it is still true these two models predict a steeper column density distribution for  $N_{\text{HI}}$  between about  $10^{12.5}$  and  $10^{14.5} \text{ cm}^{-2}$ , compared to the  $\Omega_\nu = 0.1$  CHDM models (Fig. 15).

It is not hard to understand the column density distributions of the CHDM models presented if one goes back to Fig. 13. The  $\Omega_\nu = 0.2$  models have less power than those with  $\Omega_\nu = 0.1$  on scales  $1 \text{ Mpc}^{-1} < k_S < 10 \text{ Mpc}^{-1}$ , which are relevant for the range of column densities we are interested in. As we have explained before, the column density distributions are therefore steeper for the  $\Omega_\nu = 0.2$  models at this range of column densities because they have relatively higher number of low density peaks compared to high density peaks. Among the  $\Omega_\nu = 0.2$  models, those with a lower Hubble constant produce comparatively steeper column density distributions because they have even less small scale power than the ones with a higher Hubble constant.

In Sec. 6, we have discussed how the equation of state or temperature-density relation, can change the slope of the column density distribution, although the effect is small for a reasonable range of  $\gamma$ . To demonstrate the robustness of our conclusion, we show in Fig. 19 the effects of altering the equation of state on the column density distribution for one particular CHDM model (*A2*).  $F$  is fixed at 2.5, the value that seems to give a column density distribution closest to the observational data. Smaller  $\gamma$ , as we have noted before, helps flatten the column density distribution but the flattening seems to be not quite enough even for  $\gamma = 1.2$ . We show in the same figure a dashed line with a slope of  $-1.77$  (which follows from equation (36) by putting  $\gamma = 1.2$  if one first fixes  $m$  using the case of  $\gamma = 1.5$  and  $\beta = 2$  in Fig. 16). It should be kept in mind that we can always shift the column density distribution up and down by rescaling  $F$  (Sec. 6), so the normalization is not important. It seems  $\gamma < 1.2$  is needed for this model to give the right slope of the distribution, at least the right slope to within the 95% confidence limits of the observed value (-1.37, -1.51). The same conclusion holds for the other low Hubble constant  $\Omega_\nu = 0.2$  model (*B2*). We should emphasize, however, that a more detailed comparison between the predictions of the models and observations, taking into account noise and biases of the line identification techniques, is necessary before any model can be considered ruled out.

The high Hubble constant ( $h = 0.65$ )  $\Omega_\nu = 0.2$  models *C2* and *D2*, on the other hand, have intrinsically flatter distributions and a reasonable match between theory and observations can be made by choosing  $\gamma$  in the range 1.2 – 1.7. It remains true that this class of models have steeper column density distributions compared to the CDM models previously considered for the same value of  $\gamma$ .

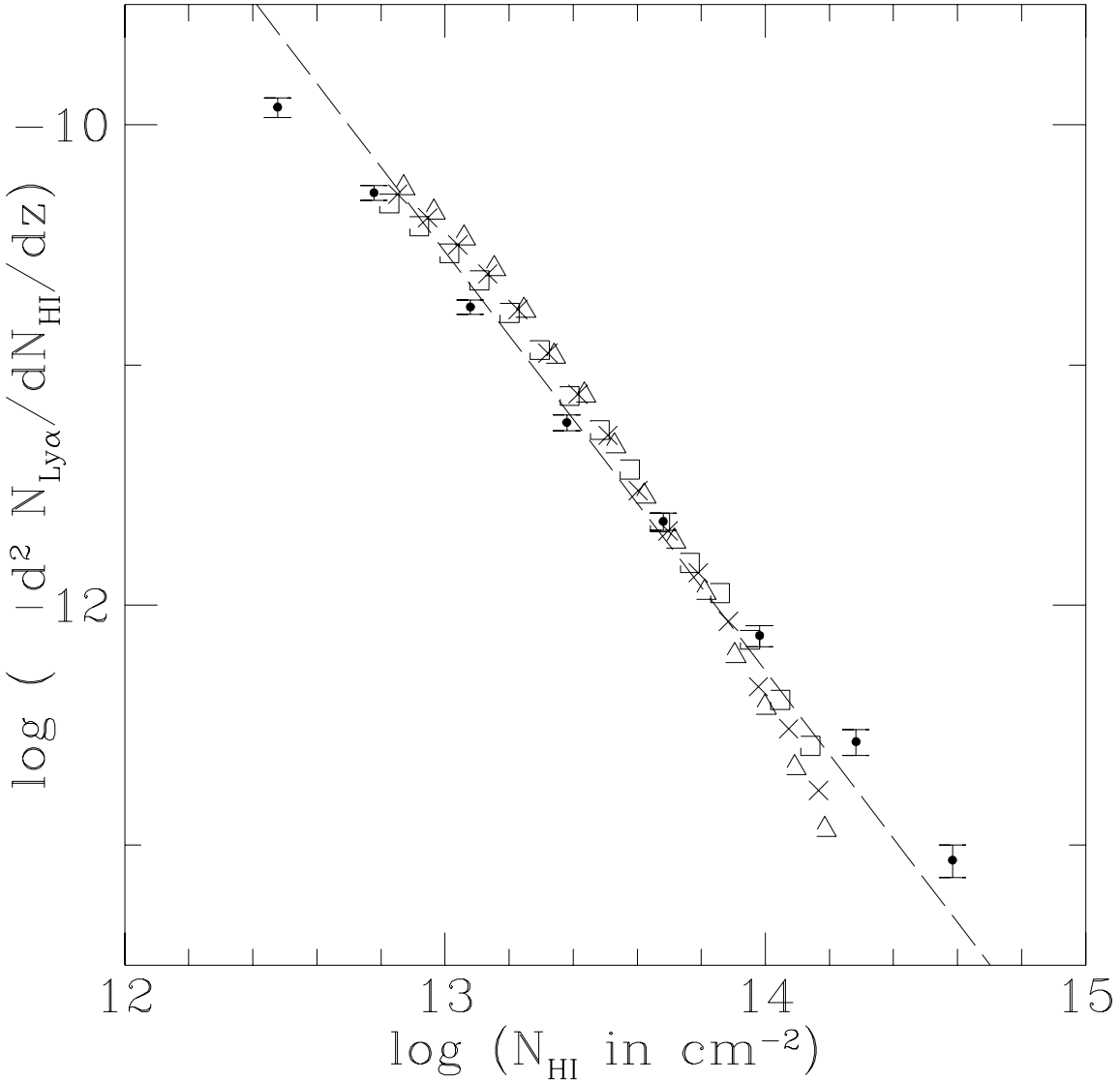


Fig. 19.— The column density distribution of the *A*2 CHDM model (Table 2) for three different values of  $\gamma$  (eq. [19]).  $F = 2.5$  (eq. [32]) is adopted. Three values of  $\gamma$  are shown:  $\gamma = 1.2$  (open squares),  $\gamma = 1.5$  (crosses) and  $\gamma = 1.7$  (open triangles). Points with error-bars are the observational data as in Fig. 7. The dashed line has a slope of  $\beta = 1.75$ , which is the value given in equation (39) for  $\gamma = 1.2$  and  $\sigma_0$  as given in Table 2.

## 9. Conclusion

We have systematically developed a set of tools to compute in an efficient manner the column density distribution given a cosmological model. One fundamental assumption of the approximations involved is that most of the Ly $\alpha$  forest with column densities in the range  $10^{12.5} - 10^{14.5} \text{ cm}^{-2}$  originate from regions of low overdensities or even underdensities which have not undergone orbit-crossing. The result of a comparison with a hydrodynamic simulation lends support to it.

One major conclusion we reach, in the process of developing the tools, is that the peculiar velocities play almost no role in determining the column density distribution at our column densities of interest, even though they are very important in determining the shapes of individual absorption line profiles. We take advantage of this fact and develop a method we call the Density-Peak-Ansatz in which each density peak is identified as an absorption line and assigned a column density based on its local properties. The column density distribution then becomes a statistic of density peaks.

In the two sections on the CDM and CHDM models, we investigate the factors controlling the column density distribution, which can be divided into two categories. One mostly affects the normalization while the other mostly influences the slope. Those that fall into the former category include the ionizing radiation intensity, the mean temperature of the intergalactic medium and the mean baryon density. Uncertainties in their values are such that almost any viable cosmological model which have the correct slope of the column density distribution can be made to match observations by a judicious choice of parameters.

The factors that mostly affect the slope of the distribution include the equation of state and more strongly so, the amount of (linear) power on scales  $1 \text{ Mpc}^{-1} \lesssim k \lesssim 10 \text{ Mpc}^{-1}$ . Models that have less power on these scales tend to have comparatively more low density peaks to high density ones and hence have relatively steeper column density distributions. Equations of state which are closer to isothermal (smaller  $\gamma$  where  $\gamma$  satisfies  $T \propto (1 + \delta_b)^{\gamma-1}$ ) tend to produce flatter column density distributions. However, within the reasonable range of  $\gamma$  (see Hui and Gnedin 1996), its precise value depending upon the reionization history, the effect of changing the equation of state is small. We put forward an approximate expression relating the slope of the column density distribution to  $\gamma$  and the power on small scales  $\sigma_0$  (eq. [39]), which describes reasonably well all the models we study in this paper.

The slope of the column density distribution provides a measure of the amount of power on small scales for a given cosmological model and given temperature-density relation. We apply our techniques to study a class of CHDM models which are known to have less power on small scales compared to other popular CDM models. We conclude that the

CHDM models indeed produce steeper column density distributions compared to the CDM models. In particular, the low Hubble constant ( $h = 0.5$ )  $\Omega_\nu = 0.2$  CHDM models, which have the least amount of power on small scales among the models we study, have column density distributions which can be made consistent with observations only for  $\gamma$  less than the values we consider reasonable. We emphasize however that only after a more detailed comparison between theories and observations, including all the effects of noise and biases of the line-identification methods, can any model be considered ruled out, based on the observed column density distribution.

We therefore conclude that a lot of work still needs to be done both on the observational and theoretical fronts. The biases of the line-identification techniques used for data reduction deserve close study so that the error bars in the observed column density distributions can be better understood and perhaps reduced. Numerical simulations on the CHDM models should be carried out to further test the accuracy of the approximations made in the present work. The effect of a fluctuating radiation field, instead of a uniform one as is assumed here, has to be investigated. Moreover, in terms of constraining models, it is also important to examine other possible statistics. We have shown, for instance, that the column density distribution is relatively independent of peculiar velocities. Are there other statistics that can take advantage of the different peculiar velocity structures predicted by different cosmological models?

In short, the study of the Ly $\alpha$  forest has entered an exciting stage. There is a gold mine of information contained in the quasar absorption spectra waiting to be discovered.

We would like to thank Edmund Bertschinger for his encouragement and many helpful comments which greatly improve the paper. It is a pleasure to thank Thomas Buchert, Lars Hernquist, Uros Seljak and Matias Zaldarriaga for useful discussions and Esther Hu for kindly sending us her data on the column density distribution. This work is supported in part by funds provided by the U.S. Department of Energy (D.O.E.) under cooperative research agreement DE-FC02-94ER40818 and in part by NSF grant AST-9318185 and NASA grant NAG5-2816.

### A. Smoothing at Jeans Scale

The effect of gas pressure is to smooth the baryon density field compared to its dark matter counterpart. The length scale below which this becomes important is the Jeans scale. In linear theory, the baryon overdensity obeys the following equation in a dark matter

dominated universe (Bi et al. 1992; Peebles 1993):

$$\frac{\partial^2 \tilde{\delta}_b}{\partial t^2} + 2H \frac{\partial \tilde{\delta}_b}{\partial t} = -4\pi G \bar{\rho}_{DM} \tilde{\delta}_{DM} + \frac{\gamma k_B \bar{T}}{\mu a^2} k^2 \tilde{\delta}_b, \quad (A1)$$

where the tilde denotes functions in Fourier space as before,  $H$  is the Hubble constant,  $k_B$  is the Boltzmann constant,  $G$  is the Newton constant,  $\bar{\rho}_{DM}$  is the average dark matter mass density,  $\bar{T}$  is the average temperature of the gas and  $\mu$  is the mean mass of each gas particle (for a fully ionized gas composed of hydrogen and helium with primordial abundances, it is about 0.6 times the proton mass). The relation between the temperature (not its average but its actual value) and  $1 + \delta_b$  is described by  $\gamma$ , the temperature being proportional to  $(1 + \delta_b)^{\gamma-1}$ .

The Jeans scale is defined in equation (16). For a dark matter dominated universe, one can replace  $\bar{\rho}_{DM}$  by the total mean density of the universe.

For the special case of  $\bar{T} \propto a^{-1}$ , making use of an equation for  $\tilde{\delta}_{DM}$  which is the same as equation (A1) except for the absence of the temperature term, it can be shown that

$$\tilde{\delta}_b(\mathbf{k}) = \frac{\tilde{\delta}_{DM}(\mathbf{k})}{(1 + k^2/k_J^2)}, \quad (A2)$$

if one ignores decaying modes. It expresses in a quantitative way the expectation that the overdensity in baryons is the same as that of dark matter on large scales (low  $k$ ) but is lower on small scales (high  $k$ ). For  $\bar{T}$  with other time dependence, solutions for equation (A1) are more complicated but the low and high  $k$  limits are the same:  $\tilde{\delta}_b = \tilde{\delta}_{DM}$  for small  $k$  and  $\tilde{\delta}_b = \tilde{\delta}_{DM} k_J^2/k^2$  for large  $k$  (Bi et al. 1992).

## B. Thermal and Ionization Evolution

The evolution of temperature is governed by:

$$\frac{dT}{dt} = -2HT + \frac{2T}{3(1 + \delta_b)} \frac{d\delta_b}{dt} - \frac{T}{\sum_i q_i} \frac{d\sum_i q_i}{dt} + \frac{2}{3k_B n_b} \frac{dQ}{dt}, \quad (B1)$$

where  $d/dt$  is the Lagrangian derivative following each fluid element,  $n_b$  is the proper number density of all gas particles and  $T$  is the temperature which depends on both space and time. The symbol  $q_i$  is defined by  $n_i \equiv (1 + \delta_b) q_i \bar{\rho}_b / m_p$ , where  $n_i$  is the proper number density of the specie  $i$ ,  $\bar{\rho}_b$  is the mean mass density of baryons at the time of interest,  $m_p$  is the mass of the proton and  $\delta_b$  is the overdensity as in equation (8). For instance the mean number density of neutral hydrogen ( $\bar{n}_H$  in equation [8]) is  $q_{HI} \bar{\rho}_b / m_p$ . The neutral fraction

of hydrogen,  $X_{\text{HI}}$  as in equation (9), is then  $q_{\text{HI}}/(q_{\text{HI}} + q_{HII})$ . Note that  $q_i$  is a function of space and time in general.

The first two terms on the right hand side take care of adiabatic cooling or heating. The third accounts for the change of internal energy due to the change in the number of particles. The last term  $dQ/dt$  is the heat gain (or negative heat loss) per unit volume by the gas particles from the surrounding radiation field. At a redshift of 2 to 4 and for densities of our interest, the main source of heat gain is photoionization and the main source of heat loss is through the recombination of ionized hydrogen and the free electron. At higher redshifts, other processes become important, such as Compton cooling. More discussion on these processes will be presented in Hui and Gnedin (1996). We note that one particularly simple solution of equation (B1) is  $T \propto a^{-2}(1 + \delta_b)^{2/3}$ , which holds when the last two terms on the right hand side can be ignored i.e. pure adiabatic expansion or compression.

The above equation has to be supplemented by one that determines the abundance of each particle type, which takes the form:

$$\frac{dq_i}{dt} = -q_i P + \sum_{j,k} q_j q_k n_b R. \quad (\text{B2})$$

For instance, if  $q_i = q_{\text{HI}}$ ,  $P$  is the photoionization rate. It is given by:

$$P = \int_{\nu_{\text{HI}}}^{\infty} 4\pi J_{\nu} \sigma_{\text{HI}} \frac{d\nu}{h\nu}, \quad (\text{B3})$$

where  $h$  is the Planck constant,  $h\nu_{\text{HI}} = 13.6$  eV,  $\sigma_{\text{HI}}$  is the cross-section for photoionization as a function of the frequency  $\nu$  and  $J_{\nu}$  is the specific intensity. The photoionization rate  $P$  depends on the normalization as well as spectrum of  $J_{\nu}$ . The specific intensity  $J_{\nu}$  is generally taken to have a power law spectrum,  $\nu^{-1}$  to  $\nu^{-1.5}$ , for frequencies just above  $\nu_{\text{HI}}$ . The spectrum at higher frequencies is less important for the photoionization rate of hydrogen. A convenient way to hide our ignorance of the spectrum is to define  $J_{\text{HI}}$  as in equation (18).

For  $q_i = q_{\text{HI}}$ ,  $R$  is the recombination rate of ionized hydrogen and the free electron ( $q_j = q_e$  and  $q_k = q_{HII}$  in equation [B3]):

$$R \sim 4 \times 10^{-13} \left( \frac{T}{10^4 K} \right)^{-0.7} \text{cm}^3 \text{s}^{-1}. \quad (\text{B4})$$

For  $J_{\text{HI}}$  with the values noted in Sec. 3.2, the photoionization time-scale is much shorter than the Hubble time. This means that hydrogen is highly ionized and is essentially

in ionization equilibrium. The two terms on the right hand side of equation (B2) almost balance each other, which implies equation (17).

We now have all the equations in place to compute the thermal and ionization evolution. The overdensity  $\delta_b$  is evolved using the Zel'dovich approximation. Its rate of growth is substituted into equation (B1), which is solved together with equation (B2). The initial conditions are as follows. The gas temperature  $T$  is equal to the cosmic microwave background temperature at  $z = 100$  (maintained by Compton scattering) and evolves adiabatically after that until the universe is reionized by the UV background. Abundances are assumed to be primordial, which is consistent with observations so far for column densities less than about  $10^{14.5} \text{ cm}^{-2}$  (See Songaila and Cowie 1996. Cooling processes due to metals are not important for our densities of interest in any case). All species are neutral until reionization occurs. One can integrate equations (B1) and (B2) forward starting from any time between  $z = 100$  and the beginning of reionization.

## REFERENCES

Bagla, J. S., & Padmanabhan, T. 1994, MNRAS, 266, 227

Bardeen, J. M., Bond, J. R., Kaiser, N., & Szalay, A. S. 1986, ApJ, 304, 15

Batjlik, S., Duncan, R., & Ostriker, J. P. 1988 ApJ, 327, 570

Bechtold, J. 1994, ApJS, 91, 1

Bi, H. G., Börner, G., & Chu, Y. 1992, A&A, 266, 1

Bi, H., Ge, J., & Fang, L.-Z. 1995, ApJ, 452, 90

Bond, J. R., Szalay, A. S. & Silk, J. 1988, ApJ, 324, 627

Brainerd, T. G., Scherrer, R. J., & Villumsen, J. V. 1993, ApJ, 418, 570

Carswell, R. F., Lanzetta, K. M., Parnell, H. C., & Webb, J. K. 1991, ApJ, 371, 36

Carswell, R. F., Webb, J. K., Baldwin, J. A., & Atwood, B 1987, ApJ, 319, 709

Cen, R., Miralda-Escudé, J., Ostriker, J. P. & Rauch, M. 1994, ApJ, 437, 9

Coles, P., Melott, A. L., & Shandarin, S. F. 1993, MNRAS, 260, 765

Cristiani, S., D'Odorico, S., Fontana, A., Giallongo, E., & Savaglio, S. 1995, MNRAS, 273, 1016

Doroshkevich, A. G. 1970, *Astrofizika*, 6, 581

Giallongo, E., Cristiani, S., D'Odorico, S., Fontana, A., & Savaglio, S. 1996, *ApJ*, 466, 46

Gnedin, N. Y., & Hui, L. 1996, preprint

Gunn, J. E., & Peterson, B. A. 1965, *ApJ*, 142, 1633

Hernquist, L., Katz, N., Weinberg, D. H., & Miralda-Escudé, J. 1995, *ApJ*, 457, L51

Hu, E., Kim, T., Cowie, L. L., Songaila, A., & Rauch, M. 1995, *ApJ*, 110, 1526

Hui, L., Bertschinger, E., 1996, accepted for publication in *ApJ* November issue

Hui, L., Gnedin, N. Y. 1996, in preparation

Hogan, C., & Rutgers, M. 1996, preprint, astro-ph 9603084

Hockney, R. W., Eastwood, J. W. 1988, *Computer Simulation Using Particles*, Bristol: Adam Hilger

Kauffmann, G., & Charlot, S. 1994, *ApJ*, 430, L97

Kofman, L., Pogosyan, D. Yu., & Shandarin, S. F. 1990, *MNRAS*, 242, 200

Kofman, L., Bertschinger, E., Gelb, J. M., Nusser, A., & Dekel, A. 1994, *ApJ*, 420, 44

Lu, L., Wolfe, A. M., & Turnshek, D. A., 1991, *ApJ*, 367, 19

Lu, L., Sargent, W. L. W., Womble, D. S., & Takada-Hidai, M. 1996, preprint, astro-ph 9606033

Ma, C.-P. 1996, preprint, astro-ph 9605198

Ma, C.-P., & Bertschinger, E. 1994, *ApJ*, 434, L5

Matarrese, S., Lucchin, F., Moscardini, L., & Saez, D. 1992, *MNRAS*, 259, 437

McGill, C. 1990, *MNRAS*, 242, 544

Meiksin, A., & Bouchet, F. R. 1995, *ApJ*, 448, L85

Melott, A. L. 1994, *ApJ*, 426, L19

Melott, A. L., Buchert, T., & Weiß, A. G. 1995, *A&A*, 294, 345

Miralda-Escudé, J., Cen, R., Ostriker, J. P., & Rauch, M. 1995, preprint, astro-ph 9511013

Mo, H. J., & Miralda-Escudé, J. 1994, ApJ, 430, L25

Murdoch, H. S., Hunstead, R. W., Petinni, M., & Blades, J. C. 1986, ApJ, 309, 19

Pando, J., & Fang, L.-Z. 1996, ApJ, 459, 1

Peebles, P. J. E. 1980, *The Large Scale Structure of the Universe*, Princeton: Princeton University Press

Peebles, P. J. E. 1993, *Principles of Physical Cosmology*, Princeton: Princeton University Press

Petitjean, P., Mücket, J. P., & Kates, R. E. 1995, å, 295, L9

Petitjean, P., Webb, J. K., Rauch, M., & Carswell, R. F., & Lanzetta, K. 1993, MNRAS, 262, 499

Press, W. H., & Rybicki, G. B. 1993, ApJ, 418, 585

Press, W. H., Rybicki, G. B., Schneider, D. P. 1993, ApJ, 414, 64

Rees, M. 1986, MNRAS, 218, 25p

Reisenegger, A., & Miralda-Escudé, J. 1995, ApJ, 449, 476

Rybicki, G. B., Lightman, A. P. 1979, *Radiative Processes in Astrophysics*, New York: Wiley

Shandarin, S. F., & Zel'dovich, Y. 1989, Rev. Mod. Phys., 61, 185

Spitzer, L. 1978, *Physical Processes in the Interstellar Medium*, New York: Wiley

Tytler, D. 1987, ApJ, 321, 49

Tytler, D. 1992, In *Statistical Challenges in Modern Astronomy*, eds. Feigelson, E. D., & Babu, G. J., New York: Springer-Verlag

Tytler, D., & Burles, S. 1996, preprint, astro-ph 9606110

Weinberg, D. H., Hernquist, L., Katz, N., & Miralda-Escudé, J. 1996, In *Cold Gas at High Redshift*, eds. Bremer, M., Rottgering, H., Carilli, C., & van der Werf, P., Kluwer: Dordrecht

Zel'dovich, Ya. B. 1970, A&A, 5, 84

Zhang, Y., Anninos, P., & Norman, M. L. 1995, ApJ, 453, L57

Zhang, Y., Anninos, P., Norman, M. L., & Meiksin, A. 1996, ApJ, in preparation